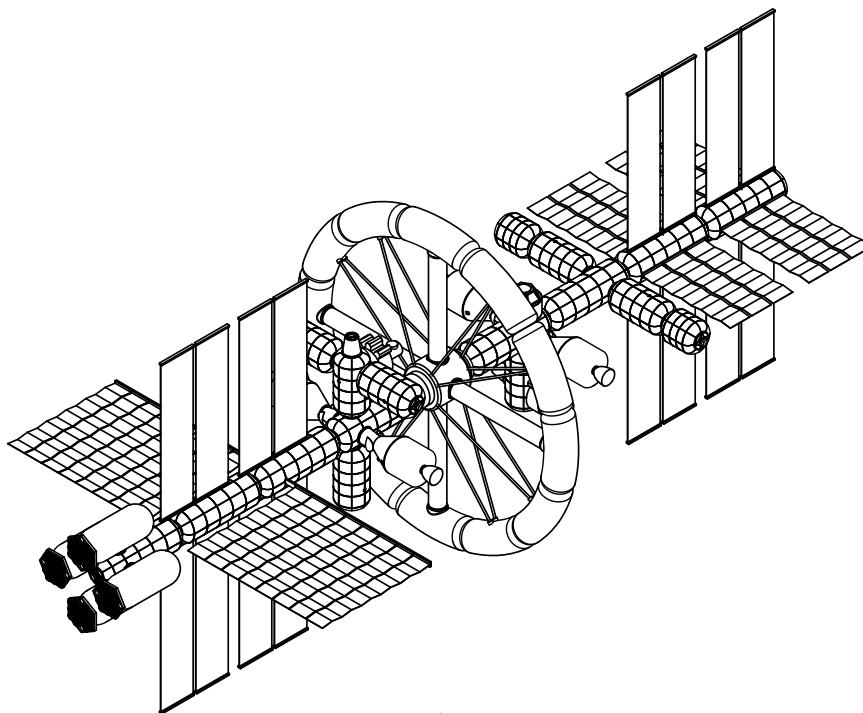# Imperial College London

# Artificial Gravity Design for the *Arceus* Mars Transit Vehicle

## *MTV03 - Spacecraft Structural Design & CAD*
### Individual Report

**Academic supervisor:** Dr Matthew Santer
**Department:** Aeronautics
**Course:** MEng in Aeronautics
**Module:** AERO96005 - GDP
**Project:** Mars Transit Vehicle
**Academic year:** 2020/2021
**Student:** Steven Dillmann
**CID:** 01518195
**Date:** 14/06/2021

Department of Aeronautics
South Kensington Campus
Imperial College London
London SW7 2AZ
U.K.

## Abstract

As part of the *Mars Transit Vehicle* Group Design Project, the Spacecraft Structural Design & CAD Team designed *Arceus*, a crewed interplanetary spacecraft capable of travelling from Earth orbit to Mars orbit. This report describes the conceptual and preliminary design stages of the rotating Artificial Gravity Ring on the spacecraft. The conceptual design defines the artificial gravity design parameters and the structural layout by assessing astronaut comfort and launch vehicle limitations. The Artificial Gravity Ring with a radius of 19 m and an angular velocity of 5.7 rpm generates an artificial gravity of 0.7 g and consists of 12 *Artificial Gravity Modules (AGMs)*, 4 *Radial Connecting Tunnels (RCTs)* and 16 *Radial Supporting Tethers (RSTs)*. The preliminary design stage involves the structural sizing and a reliability analysis of the structures based on launch and in-orbit loading conditions. Both primary structure types, *AGMs* and *RCTs*, are made out of the Aluminium-lithium alloy Al-8090 and have a structural mass of 1960 kg and 1625 kg each respectively. The secondary structures, the *RSTs*, are made out of Zylon and have a structural mass of 2.83 kg. The total structural mass of the Artificial Gravity Ring is 30065 kg.

# Contents

# List of Figures

## List of Tables

# List of Symbols

## Latin Letters

| | |
|---|---|
| $A$ | Cross-sectional area |
| $A_s$ | Stringer area |
| $a_{cent}$ | Centripetal acceleration |
| $a_{cor}$ | Coriolis acceleration |
| $A_{total}$ | Total cross-sectional area |
| $a_X$ | Longitudinal acceleration |
| $a_Y$ | Lateral acceleration |
| $b_s$ | Stringer pitch |
| $c_s$ | Stringer breadth |
| $d$ | Cross-sectional diameter |
| $D_F$ | Constant cross-section fairing diameter |
| $E$ | Elastic modulus |
| $F$ | Applied load |
| $f_{nX}$ | First longitudinal natural frequency |
| $f_{nY}$ | First lateral natural frequency |
| $F_{cr}$ | Critical cylinder buckling load |
| $F_{euler}$ | Euler buckling load |
| $g$ | Earth's gravity 9.81 m/s$^2$ |
| $h_s$ | Stringer height |
| $I$ | Second moment of area |
| $I_{total}$ | Total second moment of area |
| $k_L$ | Lethality coefficient |
| $k_x$ | Longitudinal stiffness |
| $k_y$ | Lateral stiffness |
| $k_c$ | Curved plate buckling coefficient |
| $L$ | Length |
| $L_F$ | Constant cross-section fairing height |
| $L_{eff}$ | Effective length |
| $M$ | Applied moment |
| $m$ | Launch mass |
| $m_s$ | Structural mass |
| $M_{cr}$ | Critical cylinder buckling moment |
| $m_{MAX}$ | Maximum payload mass to LEO |
| $m_{pay}$ | Payload mass |
| $m_{sh}$ | Shielding mass |

| | |
|---|---|
| $n$ | Number of modules or cuts |
| $n_s$ | Number of stringers |
| $O$ | Centre of curvature |
| $p$ | Pressure |
| $R$ | Radius of *Artificial Gravity Ring* |
| $r$ | Cross-sectional radius |
| $r_N$ | Neutral axis |
| $T$ | Tension |
| $t$ | Skin thickness |
| $t_s$ | Stringer thickness |
| $v$ | Object's relative velocity within *Artificial Gravity Ring* |
| $v_p$ | Object's relative velocity within *Artificial Gravity Ring* perpendicular to the rotation axis |
| $V_t$ | Tangential velocity of *Artificial Gravity Ring* |
| $Z_b$ | Length range parameter |

## Greek Letters

| | |
|---|---|
| $\alpha$ | Out-of plane angle of *RSTs* |
| $\gamma$ | Knockdown factor |
| $\kappa$ | Curvature |
| $\mu_F$ | Farrar efficiency |
| $\nu$ | Poisson's ratio |
| $\Omega$ | Angular velocity |
| $\rho$ | Density |
| $\sigma$ | Standard deviation |
| $\sigma_y$ | Yield or shear strength |
| $\sigma_{actual}$ | Actual stress |
| $\sigma_{allow}$ | Maximum permissible stress |
| $\sigma_{euler}$ | Euler buckling stress |
| $\sigma_{global}$ | Global cylinder buckling stress |
| $\sigma_{hoop}$ | Hoop stress |
| $\sigma_{long}$ | Longitudinal stress |
| $\sigma_{plate}$ | Local plate buckling stress |

## Abbreviations

| | |
|---|---|
| *AGM* | *Artificial Gravity Module* |
| *AG* | *Artificial Gravity* |
| FS | Factor of Safety |
| MS | Margin of Safety |

*RCT*     *Radial Connecting Tunnel*

*RST*     *Radial Supporting Tether*

*ZGM*     *Zero Gravity Module*

DLR     Deutsches Zentrum für Luft- und Raumfahrttechnik (German Aerospace Center)

ECSS    European Cooperation for Space Standardization

ESA     European Space Agency

FE      Finite Element

IMPACT  Imperial Mars Project - Advanced Crew Transit

MAST    Multi-Application Survivable Tether

MTV     Mars Transit Vehicle

NASA    National Aeronautics and Space Administration

PSD     Power Spectral Density

SDOF    Single Degree of Freedom

**Subscripts**

*b*       Bending

*c*       Compression

*cent*    centripetal/centrifugal

*cor*     Coriolis

*MAX*     Maximum

*MIN*     Minimum

*s*       Stringer

*X*       Longitudinal

*Y*       Lateral

# Conceptual Design

## 1  Introduction

### 1.1  Context and Motivation

One of the current challenges of interplanetary travel is the mitigation of adverse effects of prolonged weightlessness such as significant bone loss, muscle atrophy and cardiovascular deconditioning [6, 7]. One promising solution is *Artificial Gravity (AG)*, the simulation of gravity pull by steady rotation of all or part of the space vehicle [8]. More than a hundred years ago, the Russian space programme pioneer Konstantin Tsiolkovsky proposed the idea of generating artificial gravity with a long tether [9]; Wernher von Braun's Torus concept [10] and Gerard K. O'Neill's Cylinder concept [11] were famously adapted in Stanley Kubrick's film *2001: A Space Odyssey* and Christopher Nolan's film *Interstellar*. However, artificial gravity is not only found in science fiction. NASA proposed a truss-connected concept in 2002 [12] and the rotating wheel space station *Nautilus-X* in 2011 [13], whereas DLR and ESA are studying the effects of artificial gravity on the human body with the *Short-Arm Human Centrifuge (SAHC)* in Cologne, Germany [14].

### 1.2  Objectives

The primary objectives of the artificial gravity design are:

**(A)** Ensuring **astronaut comfort** in the *AG*-habitat.

**(B)** Structural **mass optimisation** of the *AG*-design.

**(C)** Structural **reliability assessment** of the *AG*-design.

Cost optimisation is only listed as a secondary objective as this is a government-operated mission [15].

## 2  Artificial Gravity Configuration

### 2.1  Theoretical Description of Artificial Gravity

The total acceleration due to rotation is split into two parts.

*Centripetal acceleration*
The global centripetal acceleration $a_{cent}$ is dependent on the design parameters, angular velocity $\Omega$ and radius $R$ of the *AG*-habitat. The vector form is given by Equation (2.1) and the magnitude is given by Equation (2.2). This acceleration component represents the *Design Gravity* [16].

$$\mathbf{a_{cent}} = \mathbf{\Omega} \times (\mathbf{\Omega} \times \mathbf{R}) \quad (2.1) \qquad a_{cent} = \Omega^2 R \quad (2.2)$$

*Coriolis acceleration*
The coriolis acceleration $a_{cor}$ is perpendicular to the angular velocity $\Omega$ and an object's relative velocity $v$ [17] within the *AG*-habitat. The vector form is given by Equation (2.3) and the magnitude is given by Equation (2.4), where $v_p$ is the velocity component of an object's relative velocity normal to the rotation axis of the *AG*-habitat. This acceleration component represents the *Gravity Distortion* [18] and adverse Coriolis effects [19] which define the limitations of the *AG*-habitat design as outlined in Section 2.2.

$$\mathbf{a_{cor}} = 2\mathbf{\Omega} \times \mathbf{v} \quad (2.3) \qquad a_{cor} = 2\Omega v_p \quad (2.4)$$

It is desirable to keep the ratio between Coriolis acceleration and centripetal acceleration $\frac{a_{cor}}{a_{cent}}$ low. Given a constant $a_{cor}$, decreasing $\Omega$ decreases this ratio as shown by Equation (2.5). However, for a fixed radius, decreasing $\Omega$ increases this ratio as shown by Equation (2.6), where $V_t$ is the tangential velocity of the *AG*-habitat [20].

$$\frac{a_{cor}}{a_{cent}} = \frac{2\Omega v_p}{a_{cent}} \quad (2.5) \qquad \frac{a_{cor}}{a_{cent}} = \frac{2\Omega v_p}{\Omega^2 R} = \frac{2v_p}{\Omega R} = \frac{2v_p}{V_t} \quad (2.6)$$

### 2.2  Limitations of the Artificial Gravity Habitat

To achieve objective **(A)**, the following astronaut comfort limitations have to be considered.

*Design Gravity Limits*
The design gravity $a_{cent} = \Omega^2 R$ is bounded by a lower value $a_{cent\,MIN}$, often based on studies such as human performance exxperiments on parabolic flights [21]. The upper value $a_{cent\,MAX}$ should generally not exceed the Earth's gravity g = 9.81 m/s$^2$ due to cost and comfort reasons [18].

*Maximum Angular Velocity*
Cross-coupling of head rotation and habitat rotation leads to an adverse Coriolis effect on the vestibular system [22]. This can cause nausea and dizziness, also called "motion sickness" [23]. A maximum angular velocity limit $\Omega_{MAX}$ provides mitigation of these symptoms.

*Minimum Habitat Radius*
To avoid large gravity differences between head and feet, a maximum gravity gradient $(\frac{\Delta a_{cent}}{a_{cent}})_{MAX}$ for a given radial distance difference $\Delta R$ is specified by multiple authors [24]. This allows the determination of the minimum habitat radius limit $R_{MIN}$ given by Equation (2.8).

$$\left(\frac{\Delta a_{cent}}{a_{cent}}\right)_{MAX} = \frac{\Delta R}{R_{MIN}} \quad \Longrightarrow \quad R_{MIN} = \frac{\Delta R}{\left(\frac{\Delta a_{cent}}{a_{cent}}\right)_{MAX}} \quad (2.7)$$

*Minimum Tangential Velocity*
Considering Equation (2.6), minimising the ratio of the Coriolis and centripetal acceleration can be achieved by specifying a minimum tangential velocity limit $V_{tMIN} = \Omega R$ of the *AG*-habitat given by Equation (2.8). A person walking prograde/retrograde (in the plane of rotation) with a relative velocity $v_p$ inside the rotating AG-habitat experiences a maximum percentage gravity change of $(\frac{a_{cor}}{a_{cent}})_{MAX}$.

$$\left(\frac{a_{cor}}{a_{cent}}\right)_{MAX} = \frac{2v_p}{V_{tMIN}} \quad \Longrightarrow \quad V_{tMIN} = \frac{2v_p}{\left(\frac{a_{cor}}{a_{cent}}\right)_{MAX}} \quad (2.8)$$

Table 2.1 lists comfort limits set by several different authors. Note that the authors provide values of $(\frac{\Delta a_{cent}}{a_{cent}})_{MAX}$ and $(\frac{a_{cor}}{a_{cent}})_{MAX}$ for different $\Delta R$ and $v_p$. Those two parameters presented in Table 2.1 have been scaled assuming $\Delta R = 1$ m and $v_p = 1$ m/s to allow a better comparison. For the design gravity limits of the design zone, the most conservative values of $a_{cent\,MIN} = 0.3$ g and $a_{cent\,MIN} = 0.9$ g are chosen. A maximum angular velocity of $\Omega_{MAX} = 6.0$ rpm is used as a limit, as most authors agree on this value. Recent experiments in a "slow rotation room" [32] show that at 5.4 rpm, subjects with low susceptibility performed well and by the second day were almost free from symptoms.

**Table 2.1:** Artificial gravity comfort limits set by several authors. The parameters set by the authors appear in boldface, the others derive from them [5]. The design gravity limits are given as a fraction of the Earth's gravity g = 9.81m/s$^2$.

| Author | $a_{cent\,MIN}$ [g] | $a_{cent\,MAX}$ [g] | $\Omega_{MAX}$ [rpm] | $\left(\frac{\Delta a_{cent}}{a_{cent}}\right)_{MAX}$ | $R_{MIN}$ [m] | $\left(\frac{a_{cor}}{a_{cent}}\right)_{MAX}$ | $V_{t\,MIN}$ [m/s] |
|---|---|---|---|---|---|---|---|
| Cramer, 1985 [25] | **0.1** | **1.0** | **3.0** | see Note $^a$ | - | 27 % | **7.3** |
| Stone, 1973 [26] | **0.1** | **1.0** | **6.0** | **25 %** | 4.0 | **25 %** | 9.6 |
| Gordon & Gervais, 1969 [27] | **0.2** | **1.0** | **6.0** | **8.0 %** | 12.5 | **27 %** | 7.3 |
| Gilruth, 1969 [28] | 0.3 | 0.9 $^b$ | 6.0 | 8.2 % | 12.2 | 33 % | **6.0** |
| Hill & Schnitzer, 1962 [29] | **0.04** | **1.0** | **4.0** | **6.6 %** | 15.2 | 33 % | **6.1** |
| Clark & Hardy, 1960 [30] | - | - | **0.1** | - | - | - | - |

$^a$ Author specifies an absolute gradient with respect to the Earth gravity of $(\Delta a_{cent})_{MAX} = 0.03$ g.
$^b$ Author suggests a value of $a_{cent\,MAX} = 0.9$ g to account for Coriolis acceleration raising the net acceleration above 1 g. [31]

Even more recent studies [33, 34] claim that sensory-motor adaptation to up to 10 rpm can be achieved relatively easily and quickly with training. These studies give confidence in the choice of $\Omega_{MAX}$ even though it is the least conservative one from the selection in Table 2.1. The most conservative limits of $R_{MIN}$ = 15.2 m and $V_{t\,MIN}$ = 9.6 m/s are chosen for the minimum habitat radius and minimum tangential velocity, respectively. These limits are highlighted in Table 2.1 and plotted in Figure 2.1 respectively. The shaded area represents the final *Design Zone*.
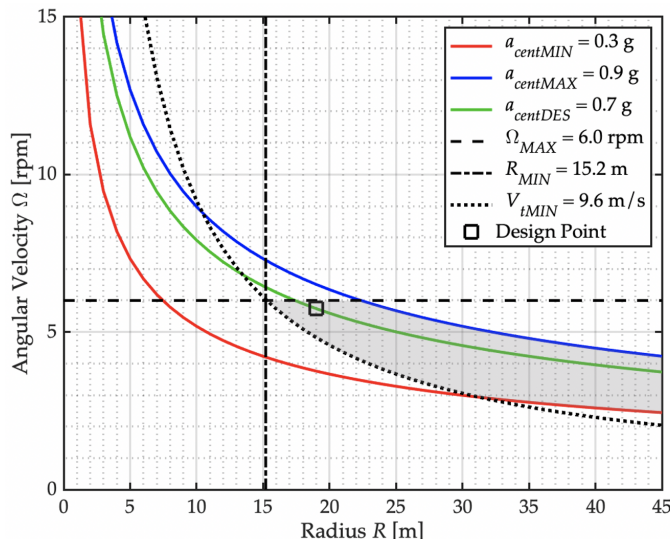


**Figure 2.1:** Artificial gravity design zone limitations.

## 2.3 Assessment of Artificial Gravity Concepts

*Rotating Cylinder*
Spinning a spacecraft around its longitudinal axis would demonstrate a simple design with small construction expenses. However, due to its short radius, it would need to spin much faster than the maximum angular velocity limit of the design zone. A large gravity gradient between head and feet is another issue to consider. Compared to large radius structures, this structural layout is also prone to destabilising effects due to its mass distribution and the dimensions of such a compact structure [35]. This configuration clearly lies outside the design zone in Figure 2.1. It does not achieve objective **(A)** and is thus ruled out.

*Tether Configuration*
The Gemini-11 mission in 1966 demonstrated a low level of artificial gravity with a 30 m tether [36]. Faster rotation or a longer tether connecting a spacecraft module to another or

to a counterweight could create substantial amount of artificial gravity within the design zone in Figure 2.1. However, the Gemini-11 experiment showed unexpected tether dynamics [37]. The difficulty in stabilising such a system due to its high number of degrees of freedom, the concern of tether breakage [38] and a number of operational problems (difficult access to modules during rotation, guidance and navigation issues etc.) [35] makes this option unattractive and is thus ruled out.

*Ring Configuration*
A ring structure rotating around a central spacecraft hub is especially attractive as it combines many advantages of the other concepts above. High achievable radii and angular velocities allow operation within the design zone in Figure 2.1, thereby achieving objective **(A)**. This configuration provides high rotational stability because its greatest moment of inertia is about the rotation axis [38]. Moreover, it has less severe operational issues than the tether configuration. Hence, a ring configuration is designed for the space vehicle of this mission. One major issue is that the ring rotation around the non-rotating part of the spacecraft leads to friction and torque causing the angular velocity to decrease [38] and make the central part of the spacecraft spin. To overcome this challenge, flywheels and extra thrusters are needed which are discussed in a separate report by MTV04 [39].

To determine the *AG Design Point*, i.e. the combination of radius $R$ and angular velocity $\Omega$, a design gravity of $a_{cent}$ = 0.7 g is chosen as it is a widely accepted value in the artificial gravity research field [40, 41]. To minimise mass and thus follow objective **(B)**, the volume and hence radius should be kept low whilst satisfying the human comfort limitations. Hence, a design point along the $a_{cent}$ = 0.7 g line (———) on the left of the design zone in Figure 2.1 is chosen. The final design parameters are a radius of $R$ = 19 m and an angular velocity of $\Omega$ = 5.7 rpm to allow a 5 % margin from the motion sickness limit of $\Omega_{MAX}$ = 6.0 rpm.

## 2.4 Launch Considerations

The restricted size of payload fairings inside of launch vehicles would only allow launching separate modules for the artificial gravity ring. On-orbit assembly of the modules at LEO is required to build the closed ring structure. The final artificial gravity ring consists of thin-walled curved modules with circular cross-section, which is ideal in taking pressurisation loads. Moreover, this cross-section

uses the payload fairing space inside the launch vehicles most efficiently. It is desirable to keep the number of modules low to reduce the construction time and launch costs, as discussed in a separate report by MTV02 [42].

**Table 2.2:** Launch capabilities of existing launch vehicles.

| Launch Vehicle | $m_{MAX}$ [t] | $L_F$ [m] | $D_F$ [m] |
|---|---|---|---|
| Ariane 6 [43] | 21.7 | 11.2 | 4.6 |
| Ariane 5 [44] | 21.0 | 10.1 | 4.6 |
| Atlas V [45] | 18.5 | 12.2 | 4.6 |
| Delta IV Heavy [46] | 28.8 | 11.3 | 4.6 |
| Falcon Heavy [47] | 18.1 | 6.7 | 4.6 |
| Soyuz [48] | 7.8 | 5.1 | 4.1 |

The launch vehicle capabilities affect the number of modules $n$ and limit their outer dimensions, i.e. length $L$ and radius $r$. This analysis is conducted based on geometric launch limitations, i.e. the constant cross-section fairing height $L_F$ and diameter $D_F$. These are tabulated in Table 2.2 for different launch vehicles. The maximum payload mass $m_{MAX}$ to LEO is considered in the preliminary design. To ensure geometrical compatibility for the simplified module and launch fairing geometry in Figure 2.2, the relations given by Equations (2.9), (2.10) and (2.11) must hold [49].
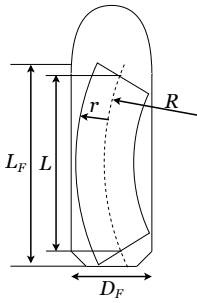


$$L = 2R\sin\frac{\pi}{n} \quad (2.9)$$

$$2(R + r)\sin\frac{\pi}{n} \leq L_F \quad (2.10)$$

$$(R + r) - (R - r)\cos\frac{\pi}{n} \leq D_F \quad (2.11)$$

**Figure 2.2:** Simplified geometry of one artificial gravity module inside a launcher payload fairing.

For a ring radius of $R = 19$ m, the minimum required number of modules $n$ are plotted against a range of module radii $r$ for different launch vehicles in Figure 2.3. For this ring radius, a minimum cross-sectional module radius of $r_{MIN} = 1.8$ m is dictated by payload and crew space requirements, as discussed in a separate report by MTV06 [50]. The Soyuz and Falcon Heavy would require substantially more modules to be launched. For radii of $r > 2$ m, the number of launches required increase sharply for the Ariane 5, Ariane 6, Delta IV Heavy and Atlas V launchers. For radii of $r \leq 2$ m, the Ariane 6, Delta IV Heavy and Atlas V launchers are capable of launching the artificial gravity ring with 12 launches. Hence, the number of modules is chosen to be $n = 12$. Allowing an extra 10 cm stand-off distance for the Whipple shields discussed in a separate report by MTV06 [51], gives a maximum module radius of $r = 1.9$ m with an acceptable margin of 5 % from $r_{MIN}$. Using Equation (2.9) and accounting for about 4 cm space for the module interfaces yields a module length of $L = 9.8$ m. The artificial gravity habitats are connected to the central part of the spacecraft by tunnels of length $L = 14$ m and a cross-section radius of $r = 1.2$ m with a Whipple shield stand-off distance of 15 cm [51] which requires using the space in the nose cone of the launch vehicles.
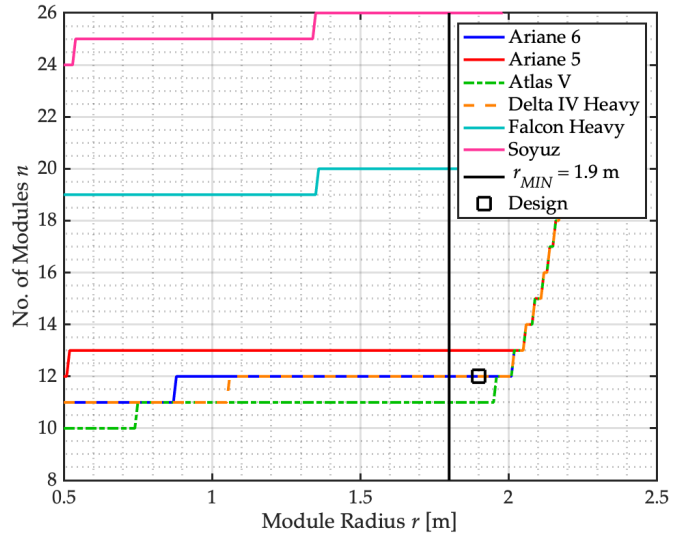


**Figure 2.3:** Number of launches required for the artificial gravity ring for different module radii.

## 2.5   Structural Layout

The mission's spacecraft is named *Arceus* and consists of four main structural components.
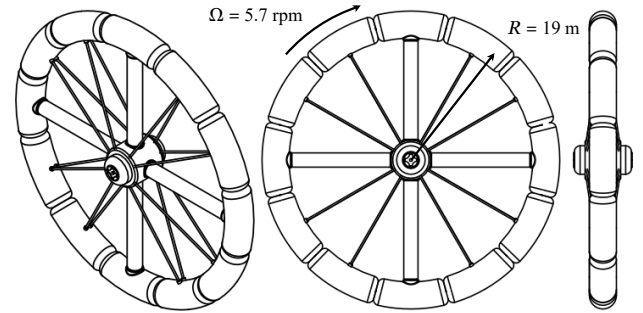


**Figure 2.4:** Layout of the *Artificial Gravity Ring* on *Arceus* designed with *CATIA V5*.

*Zero Gravity Modules (ZGMs)* These modules constitute the central non-rotating part of the spacecraft, the *ZG-Body*. Their main purpose is to accommodate the subsystems of the spacecraft.

*Artificial Gravity Modules (AGMs)* $\times 12$
These modules constitute the outer rotating part of the spacecraft, the *AG-Ring*. They provide continuous artificial gravity and living space for the astronauts.

*Radial Connecting Tunnels (RCTs)* $\times 4$
These structures connect the *ZG-Body* to the *AG-Ring*. They allow transition between the rotating and non-rotating parts of the spacecraft.

*Sizing of Secondary Structures* $\times 16$
These tethers run from the *ZG-Body* to the *AG-Ring* at an angle of 7.5° out of the rotation plane on each side. They support the *RCTs* in taking tensile centrifugal loads and provide a stiffening effect against ring oscillations.

The structures sized and analysed in this report are the *AGMs* and *RCTs* (primary structures) as well as the *RSTs* (secondary structure). The *ZGMs* including the bearing system structures are discussed in a separate report [52].

# Preliminary Design

## 3   Sizing of Primary Structures

### 3.1   Design Loading Conditions

The primary structures are sized and analysed based on the following loading conditions.

*Load Case 1: Quasi-static Loads, Natural Frequencies*
During launch, a spacecraft experiences a range of lateral and axial accelerations. Maximum quasi-static loads are specified in launch vehicle user manuals for different launch stages. These are a combination of the steady-state static loads and the low frequency sinusoidal loads [53]. A longitudinal acceleration of $a_X = 6\,\mathrm{g}$ and lateral acceleration of $a_Y = \pm 2\,\mathrm{g}$, applied at the centre of mass, are chosen for the design of the spacecraft modules. These values represent upper bounds of the values given in Table 3.1.

**Table 3.1:** Maximum quasi-static loads and minimum stiffness requirements for the chosen launch vehicles.

| Launch Vehicle | $a_X$ [g] | $a_Y$ [g] | $f_{nX}$ [Hz] | $f_{nY}$ [Hz] |
|---|---|---|---|---|
| Ariane 6 [43] | 4.6 | ±2.0 | ≥ 20 | ≥ 6 |
| Atlas V [45] | 6.0 | ±2.0 | ≥ 15 | ≥ 8 |
| Delta IV Heavy [46] | 6.0 | ±2.0 | ≥ 30 | ≥ 8 |

These design load factors are only applicable if the stiffness requirements are satisfied: To prevent dynamic coupling of the spacecraft with the launch vehicle, the fundamental natural (undamped) frequencies of the spacecraft must be larger than the lowest frequencies generated by the launch vehicle that excite the spacecraft [53]. Table 3.1 shows the minimum natural frequency requirements of the spacecraft for different launch vehicles in the longitudinal direction $f_{nX}$ and lateral direction $f_{nY}$ assuming that the spacecraft is cantilevered at the payload fairing interface. The most conservative values of $f_{nX} \geq 30\,\mathrm{Hz}$ and $f_{nY} \geq 8\,\mathrm{Hz}$ are chosen for the design of the spacecraft modules.

*Load Case 2: Pressurisation*
In-orbit pressurisation of the *AGMs* and *RCTs* with a magnitude of $p = 1\,\mathrm{atm} = 101.325\,\mathrm{kPa}$.

*Load Case 3: Rotation*
In-orbit rotation of the *AG-Ring* with a radius of $R = 19\,\mathrm{m}$ and an angular velocity of $\Omega = 5.7\,\mathrm{rpm} = 0.597\,\mathrm{rad/s}$ to provide a design gravity of $a_{cent} = 0.7\,\mathrm{g}$ inside of the *AGMs*.

*Load Case 4: Spin-Up and Spin-Down*
In-orbit 5-hours spin-up and spin-down of the *AG-Ring* from 0 rpm to 5.7 rpm with four electric propulsion thrusters placed at a radial distance of 22 m from the rotation axis, each providing a thrust of 5.4 N [54].

*Load Case 5: Thrust acceleration*
In-orbit maximum thrust acceleration of $0.40\,\mathrm{mm/s^2}$ on *Arceus* [55].

### 3.2   Failure Mechanisms

In this analytical sizing procedure, it is assumed that the structures may fail due to the following mechanisms.

*Yield and Shear Failure*
The structures fail if the tensile, compressive or shear stress reaches the yield/shear strength $\sigma_y$ of the material.

*Global Euler Buckling*
The classical Euler buckling load $F_{euler}$ for a slender column is given by Equation (3.1), where the effective length is $L_{eff} = 2L$ for a column of length $L$, elastic modulus $E$, second moment of area $I$ and a fixed boundary condition at one end. The Euler buckling stress $\sigma_{euler}$ given by Equation (3.2). is found by dividing $F_{euler}$ by the cross-sectional area $A$.

$$F_{euler} = \frac{\pi^2 EI}{L_{eff}^2} \quad (3.1) \qquad \sigma_{euler} = \frac{F_{euler}}{A} = \frac{\pi^2 EI}{L_{eff}^2 A} \quad (3.2)$$

*Global Cylinder Buckling*
Cylindrical shells are often thin enough to buckle before yield failure occurs, and often too short to buckle as Euler columns [56]. Donnell's thin cylindrical shell buckling theory [57] predicts the critical buckling stress $\sigma_{global}$ given by Equation (3.3) of a thin cylinder shell with radius $r$, thickness $t$ and Poisson's ratio $v$. However, experimental results of thin cylinder shells show significantly lower buckling loads than the theoretical prediction due to their extreme sensitivity to imperfections under axial compression [58]. In practice, a knockdown factor $\gamma$ included in Equation (3.3) is used. The knockdown factor $\gamma_c$ recommended by [59] in Equation (3.5) provides a good lower bound based on empirical data, where $\phi$ is given by Equation (3.4).

$$\sigma_{global} = \frac{\gamma E}{\sqrt{3(1-v^2)}} \frac{t}{r} \quad (3.3) \qquad \phi = \frac{1}{16}\sqrt{\frac{r}{t}} \quad (3.4)$$

$$\gamma_c = 1 - 0.901(1 - e^{-\phi}) \quad (3.5) \quad \gamma_b = 1 - 0.731(1 - e^{-\phi}) \quad (3.6)$$

It was shown by [60] that the critical buckling stress prediction of a thin-walled cylinder subjected to pure bending was approximately equal to that of a thin-walled cylinder subjected to axial compression. However, experimental results show that cylinders are less sensitive to imperfections [61] in bending. Thus, a smaller knockdown factor $\gamma_b$ suggested by [62] in Equation (3.6) is used here. In many cases, aerospace structures are subjected to combined loading. A common conservative practice is to assume that the structure will fail when the sum of the different critical load ratios are equal to unity [61]. The critical load $F_{cr}$ for axial compression and critical moment $M_{cr}$ for bending are given by Equations (3.7) and (3.8). The interaction failure criterion is found using Equations (3.9) and (3.10).

$$F_{cr} = 2\pi r t \sigma_{global} = \frac{\gamma_c E}{\sqrt{3(1-v^2)}} 2\pi t^2 \quad (3.7)$$

$$M_{cr} = \pi r^2 t \sigma_{global} = \frac{\gamma_b E}{\sqrt{3(1-v^2)}} \pi t^2 r \quad (3.8)$$

$$R_c + R_b = 1 \quad (3.9) \qquad R_c = \frac{F}{F_{cr}} \ \ \& \ \ R_b = \frac{M}{M_{cr}} \quad (3.10)$$

*Local Plate Buckling*
Thin cylindrical shell structures are used for many aerospace structures such as aircraft fuselages or rockets. Often, global buckling is the design driver [63]. Circumferential and longitudinal stiffening with rings and stringers

are used to avoid premature failure and to reduce the structural mass. However, local buckling failure of the individual plates may occur. A stiffened thin-walled cylinder shell consist of curved plates with thickness $t$ and width $b_s$ for which the buckling stress $\sigma_{plate}$ is given by Equation (3.11) [2]. The compressive buckling coefficient $k_c$ is found from Figure 7.1 in Appendix A and depends on the length range parameter $Z_b$ given by Equation (3.12).

$$\sigma_{plate} = \frac{k_c \pi^2 E}{12(1-v^2)}\left(\frac{t}{b_s}\right)^2 \quad (3.11) \qquad Z_b = \frac{b_s^2\sqrt{1-v^2}}{rt} \quad (3.12)$$

*Local Stringer Buckling*
Introducing stringers may also cause flexural instability (Euler buckling) of the individual stringers. Skin-stringer panels are considered structurally efficient when local plate and stringer buckling occur at the same time. This is characterised by the Farrar efficiency $\mu_F$.

## 3.3  Material Selection

The following material selection is based on commonly used Aluminium, Titanium and Stainless steel alloys. Thin-walled cylinder shells are much more likely to fail by buckling rather than by yielding. Moreover, satisfying the previously mentioned stiffness requirement (minimum natural frequencies) is important. Hence, maximising the elastic modulus $E$ is favourable. Moreover, minimising density $\rho$ is desirable to follow objective **(B)**. As a measure of the structural efficiency, define the material index $M_c$ given by Equation (3.13) for beams, plates and shells in compression. For buckling and bending problems of beams, plates and shells, the material index $M_b$ is defined by Equation (3.14) [64].

$$M_c = \frac{E}{\rho} \qquad (3.13) \qquad M_b = \frac{E^{\frac{1}{2}}}{\rho} \qquad (3.14)$$

The optimal material is found by maximising $M_c$ and $M_b$ with an Ashby Chart in Figure 3.1 produced with the CES material selection software [65].
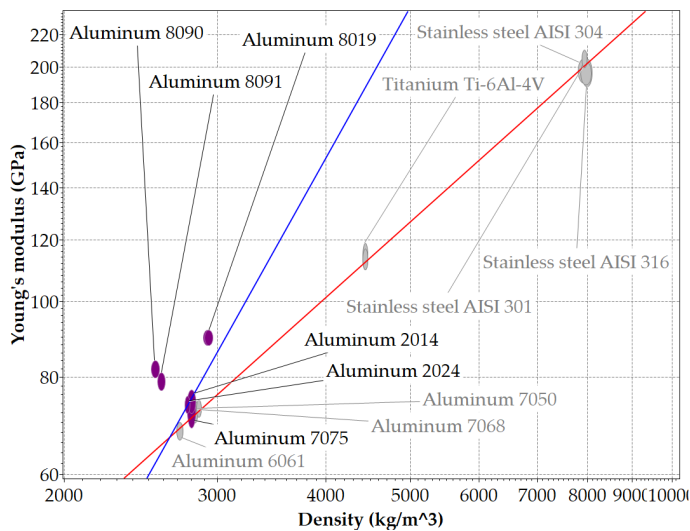


**Figure 3.1:** Ashby chart for $M_c$ and $M_b$ with design guidelines of slopes 1 (red) and 2 (blue) respectively.

All alloy groups perform similarly well with respect to $M_c$. However, Aluminium alloys perform better with respect to $M_b$. In both cases, the Aluminium-lithium alloy Al-8090 performs the best and is thus selected for both primary structures. Its properties are summarised in Table 3.2. Aluminium-lithium alloys have been developed to reduce the weight of aerospace structures. The chosen alloy has a low density, a high elastic modulus and excellent fatigue properties. It has a significantly higher strength and toughness at cryogenic temperatures than conventional Aluminium alloys such as the Al-2024 alloy.

**Table 3.2:** Important design properties of Al-8090 T851.

| Material | $\rho$ [kg/m$^3$] | $\sigma_y$ [MPa] | $E$ [GPa] | $v$ |
|---|---|---|---|---|
| Al-8090 T851 | 2550 | 440 | 84 | 0.33 |

## 3.4  Sizing Procedure

The *AGMs* and *RCTs* are sized to withstand **Load Case 1** as the in-orbit loads are relatively small.

*Factor of Safety*
A safety factor of $FS = 2.5$ is chosen based on the *ECSS* design logic outlined in Appendix B. The safety factor is not shown in the formulae in the next paragraph, but is used to obtain any final results presented in Section 3.5.

*Load Modelling*
The quasi-static loads are given by

$$a_X = 6\,g \quad \& \quad a_Y = \pm 2\,g$$

and are defined to act through the centre of mass, as illustrated in Figure 3.2.
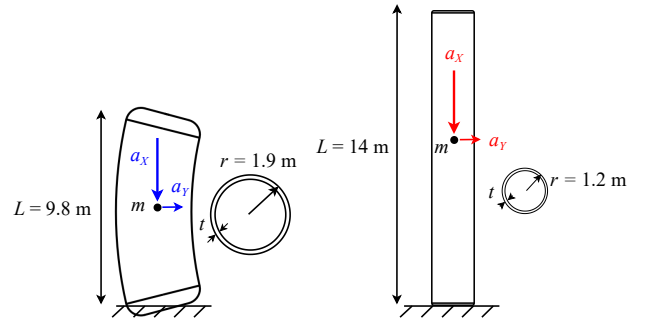


**Figure 3.2:** Quasi-static loads on *AGMs* and *RCTs*.

The launch mass $m$ is the sum of the structural mass $m_s$ and shielding mass $m_{sh}$. The shielding mass $m_{sh}$ is given in Table 3.3 in Section 3.5 and is discussed in a separate report by MTV06 [51]. The longitudinal and lateral point forces are

$$F_X = m \cdot a_X = m \cdot 6\,g \quad \& \quad F_Y = m \cdot a_Y = \pm m \cdot 2\,g$$

The bending moment due to the lateral force $F_Y$ is given by

$$M(x) = \begin{cases} F_Y(L/2 - x) & 0 \le x \le L/2 \\ 0 & L/2 \le x \le L \end{cases}$$

where $x$ is the abscissa along the length $L$. As the *AGMs* are curved, Winkler's Theory for initially curved beams in bending [66] is used to obtain the stress due to the lateral force $F_Y$. The neutral axis $r_N$ given by Equation (3.16) shifts closer to centre of curvature $O$, away from the centroid by a distance $e$ given by Equation (4.1) [67], where $s$ is any radial position from the centre of curvature $O$, $R$ is the radius

of curvature and $A$ is the cross-sectional area.

$$e = R - r_N \quad (3.15) \qquad r_N = \frac{A}{\int_A \frac{dA}{s}} \quad (3.16)$$

Following the derivation in [67], Equation (3.17) gives the tangential stress $\sigma_1(x)$ in a curved beam subjected to bending at a distance $s$ away from the centre of curvature $O$.

$$\sigma_1(x) = \frac{M(x)(r_N - s)}{Aes} \quad (3.17) \qquad \sigma_1(x) = \frac{M(x)c}{I} \quad (3.18)$$

The *RCTs* are straight and the bending stress due to the lateral force $F_Y$ can be found using the Engineer's Theory of Bending (ETB) with Equation (3.18), where $c$ is the distance from the neutral axis (here also the centroid) and $I$ is the second moment of area of the cross-section. Assuming that the *AGMs* behave as straight cylinders in axial compression, the axial compressive stress in both structures due to the longitudinal load is simply given by $\sigma_2 = F_Y/A$. This gives the total maximum compressive stress at the clamped end interface $\sigma_{max} = \sigma_1(0) + \sigma_2$ for $s = c = r$, where $r$ is the cross-section radius of the thin-walled cylinder. The maximum transverse shear stress for a thin-walled cylinder in bending is given by Equation (3.19).

$$\tau_{max} = \frac{2F_Y}{A} \quad (3.19)$$

*Stiffness Requirements (Natural Frequencies)*
To prevent dynamic coupling between spacecraft and launch vehicle, the stiffness requirements at launch

$$f_{nX} \geq 30\,\text{Hz} \quad \& \quad f_{nY} \geq 8\,\text{Hz}$$

must be satisfied. Assume that both structures behave as SDOF systems with their mass $m$ concentrated at the centre of mass. The first longitudinal and lateral natural frequencies, $f_{nX}$ and $f_{nY}$, of a clamped beam are given by Equations (3.20) and (3.21) considering its longitudinal stiffness $k_x = \frac{EA}{L}$ and lateral stiffness $k_y = \frac{3EI}{L^3}$ [68, 69].

$$f_{nX} = \frac{1}{2\pi}\sqrt{\frac{k_x}{m}} = \frac{1}{2\pi}\sqrt{\frac{EA}{Lm}} \quad (3.20)$$

$$f_{nY} = \frac{1}{2\pi}\sqrt{\frac{k_y}{m}} = \frac{1}{2\pi}\sqrt{\frac{3EI}{L^3 m}} \quad (3.21)$$

*Skin Stringer Design*
Cylindrical shells are unstable when loaded in compression and bending. The skin has to be made relatively thick in order to avoid global cylinder buckling. This makes monocoque shells inefficient, leading to a significant mass penalty. Supporting thin shells with stiffening stringers allows reducing the skin thickness and mass of the spacecraft, thus achieving objective **(B)**. Given the high structural efficiency to high loads, the primary structures are designed as semi-monocoque structures, i.e. thin-walled circular cylinders stiffened with longitudinal stringers. If global Euler buckling becomes constraining, circumferential rings are introduced to reduce the effective length.

*Stringer Geometry and Dimensions*
Different stringer geometries are used in practice depending on the application. Z-stringers of height $h_s$, breadth $c_s$ and thickness $t_s$ are chosen due to their high structural efficiency in high stress applications [70]. The stringer pitch $b_s$ depends on the number of stringers $n_s$ and the cylinder radius $r$ given by Equation (3.22) and the stringer cross-sectional area is given by Equation (3.23).

$$b_s = \frac{2\pi r}{n_s + 1} \quad (3.22) \qquad A_s = t_s(h_s + 2c_s) \quad (3.23)$$

As a measure of the structural efficiency of the skin-stringer construction, the Farrar efficiency $\mu_F$ [3] is commonly used in the design of aerospace structures, which is a function of the stringer to skin thickness ratio $t_s/t$ and the ratio of stringer area to the product of stringer pitch and skin thickness $\frac{A_s}{b_s t}$. Often, the stringers will not develop flexural instability. However, for analysis, flexural instability is assumed to occur [71]. If that is the case, an optimum value of these parameters exists to ensure that local plate and local stringer buckling occurs at the same time [3]. Choosing a stringer breadth to height ratio of $c_s/h_s = 0.3$ and thus $h_s = 0.625\frac{A_s}{t_s}$ allows using the Farrar efficiency design chart for Z-stringers in Figure 7.2 in Appendix A, which gives optimal ratios of $t_s/t = 1.05$ and $\frac{A_s}{b_s t} = 1.5$ for the maximum Farrar efficiency of $\mu_F = 0.95$ [3]. However, the stiffening ratio $\frac{A_s}{b_s t}$ is much higher than the ones found in industry practice because higher skin thicknesses are required, for example for pressurisation [71]. A stiffening ratio usually found in practice of $\frac{A_s}{b_s t} = 0.3$ is chosen. To achieve a Farrar efficiency of around $\mu_F = 0.7$, this requires a thickness ratio of $t_s/t = 0.7$. For a specified number of stringers $n_s$ and a given skin thickness $t$, all stringer dimensions can now be evaluated given the ratios mentioned above.

*Mass Optimisation Methodology*
Having established the stringer dimensions in terms of the number of stringers $n_s$ and skin thickness $t$, the mass optimisation methodology is based on iterating over different number of stringers $n_s$. The design logic relies on sizing the structure based on local plate buckling whilst ensuring that no other failure mechanisms occur and that the stiffness requirements are met. Increasing the number of stringers $n_s$, allows a lower skin thickness $t$ and lower structural mass $m_s$. The minimum mass design and thus objective **(B)** is achieved by selecting the number of stringers $n_s$ and skin thickness $t$ at which another failure mechanism occurs, or the stiffness requirements are violated. The detailed methodology is as follows:

1. Specify the number of stringers $n_s$ (start with $n_s = 0$) and evaluate the equivalent stringer pitch $b_s$ with Equation (3.22).

2. Find the maximum applied compressive load $F$ and bending moment $M$ and thus the maximum compressive stress $\sigma_{max}$ (see Load Modelling paragraph).

3. Equate the applied compressive stress to the local plate buckling stress in Equation (3.11) to find the required skin thickness $t$.

$$\sigma_{max} = \sigma_{plate} \implies t = \sqrt{\frac{12(1 - \nu^2)\sigma_{max}}{k_c \pi^2 E}}\, b_s$$

4. Calculate the stringer dimensions with

$$t_s = 0.7t \quad A_s = 0.3b_s t \quad h_s = 0.625\frac{A_s}{t_s} \quad c_s = 0.3h_s$$

5. Find the structural mass $m_s$ for the given number of

stringers $n_s$, where $L$ is the length of the cylinder and $A_{total}$ is the total cross-sectional area of the skin-stringer construction with

$$m_s = \rho A_{total} L = \rho(2\pi r t + n_s A_s) L$$

6. Define the effective thickness $t_{eff}$ by the "smearing approximation" with

$$t_{eff} = t + \frac{A_s}{b_s}$$

7. Use $t_{eff}$ together with Equations (3.7) and (3.8) to find the critical load $F_{cr}$ and critical moment $M_{cr}$ and thus $R_c$ and $R_b$. Then check the global cylinder buckling interaction criterion given by Equation (3.9).

   (a) If $R_c + R_b < 1$:
       Increase the number of stringers $n_s$ and start from Step 1 again.

   (b) If $R_c + R_b \geq 1$:
       Stop iterating. The previous iteration gives the minimum mass design.

Euler buckling, yield/shear failure have also been considered in the iteration in Step 7 but are not as constraining as global cylinder buckling stress which decreases with decreasing thickness. Moreover, the natural frequencies evaluated at each iteration to ensure that the stiffness requirements are met. For these considerations, the second moment of area $I_{total}$ of the skin-stringer construction is required and is evaluated at each iteration. Note that the loading depends on the structural mass $m_s$ which is yet to be found. This issue is solved by making an initial guess of the skin thickness and hence mass, followed by an iteration until the mass converges to within 1 %.

## 3.5   Sizing Results

### Design Results

Following the design procedure outlined in the previous subsection, the applied maximum stress (equal to local plate buckling stress) for a range of number of stringers is plotted in Figure 3.3 for both *AGMs* (——) and *RCTs* (——).
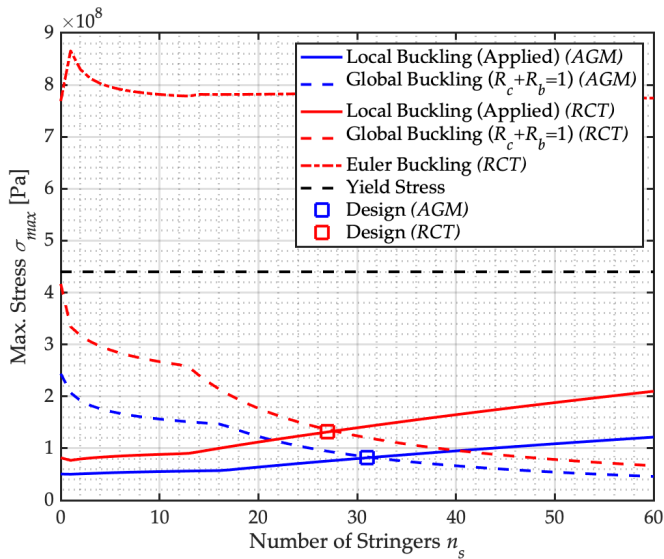
The applied stress is compared to the global cylinder buckling, Euler buckling and yield stress. Note that the Euler buckling stress of the *AGMs* is not plotted due to its higher order magnitude of around 3.9 GPa at $n_s = 30$. The same holds for the shear stress for both structures due to its lower order magnitude of around 19 MPa at $n_s = 30$. As expected, global buckling failure is more constraining than yield or Euler instability. The discontinuity in the graphs are due to the change of the curved plate buckling coefficient $k_c$ as a function of the plate length range parameter $Z_b$, see Figure 7.1 in Appendix A. The design point is defined as the point at which global cylinder and local plate buckling occur at the same time corresponding to the minimum mass design as shown in Figure 3.4.
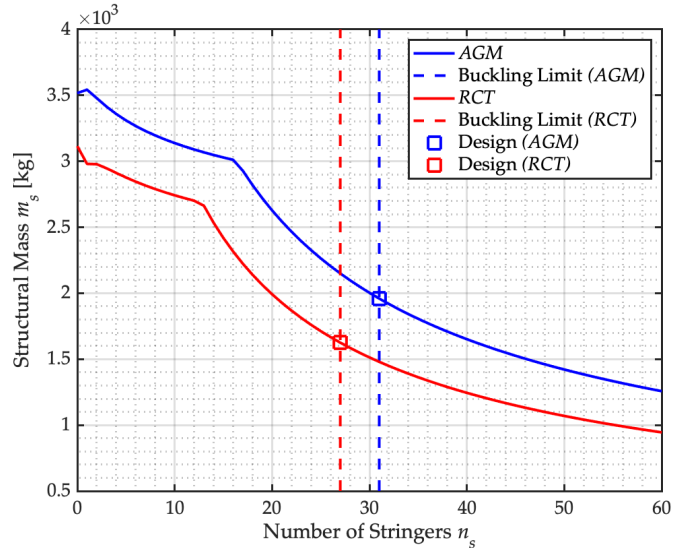


**Figure 3.4:** Mass variation with number of stringers.

The first longitudinal and lateral natural frequencies, $f_{nX}$ and $f_{nY}$ of the spacecraft are evaluated using Equations (3.20) and (3.21) from the previous subsection. As shown in Figure 3.5, the longitudinal and lateral stiffness requirements $f_{nX} \geq 30$ Hz and $f_{nY} \geq 8$ Hz are satisfied by both *AGMs* and *RCTs*.



**Figure 3.3:** Maximum compressive stress at the payload adapter interface compared to failure stresses.



**Figure 3.5:** First longitudinal and lateral frequency variation with number of stringers.

*Design Summary*
The final results are summarised in Table 3.3.

**Table 3.3:** Summary of the skin-stringer panel geometries.

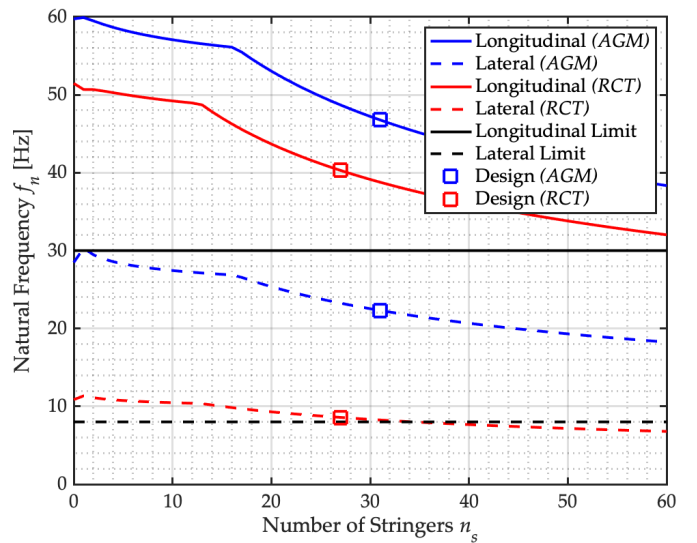| Structure | AGMs | RCTs |
|---|---|---|
| Length $L$ [m] | 9.8 | 14 |
| Radius $r$ [m] | 1.9 | 1.2 |
| Curvature $\kappa$ [1/m] | 0.053 | 0 |
| Number of Stringers $n_s$ | 31 | 27 |
| Skin Thickness $t$ [mm] | 5.1 | 4.7 |
| Stringer Thickness $t_s$ [mm] | 3.6 | 3.3 |
| Stringer Height $h_s$ [cm] | 10 | 7.2 |
| Stringer Breadth $c_s$ [cm] | 3.0 | 2.2 |
| Stringer Pitch $b_s$ [cm] | 37.3 | 26.9 |
| Effective Thickness $t_{eff}$ [mm] | 6.6 | 6.1 |
| Stringer Area $A_s$ [mm$^2$] | 569 | 384 |
| Total Cross-sectional Area $A_{total}$ [cm$^2$] | 783 | 455 |
| Total 2nd Moment of Area $I_{total}$ [dm$^4$] | 1429 | 337 |
| First Longitudinal Nat. Frequency $f_{nX}$ [Hz] | 46.8 | 40.3 |
| First Lateral Nat. Frequency $f_{nY}$ [Hz] | 22.3 | 8.6 |
| Structural Mass $m_s$ [kg] | 1960 | 1625 |
| Shielding Mass $m_{sh}$ [kg] [51] | 13601 | 6896 |
| Total Launch Mass $m$ [kg] | 15561 | 8521 |

The total launch masses are well below the maximum payload masses $m_{MAX}$ in Table 2.2 in Section 2.4. The same analysis with the Titanium alloy Ti-6Al-4V gives structural masses of 3313 kg and 2793 kg for the *AGMs* and *RCTs*. This supports the material choice according to objective **(B)**.

## 3.6   Finite Element Analysis

The analytical results are compared to Finite Elements (FE) results obtained with *ABAQUS*. Both *AGMs* and *RCTs* are modelled as linear quadrilateral 3D shell elements as they are commonly used in thin-walled cylinder buckling problems. Triangular shell elements have displayed shear locking issues in the past [61]. The shells are clamped at the bottom edge modelled with an "encastre" boundary condition. The smeared stiffener theory allows the sized stringers to be smeared along the thickness of the shell.

*Maximum Compressive Stress Comparison*
The find the maximum stress on the compression surface as shown by Figure 3.6, gravity loads of $-6\,g \cdot FS$ and $2\,g \cdot FS$ are applied in the longitudinal and lateral directions respectively. The same safety factor of $FS = 2.5$ is used.
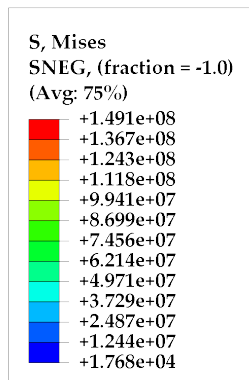
As shown by Figure 3.7, a convergence test for both *AGM* and *RCT* models is conducted by refining the mesh from 10 to 150 edge seeds in steps of 10 until the stress predictions converge to within 1 %. The *RCT* model converges in a smoother and quicker manner than the *AGM* model.
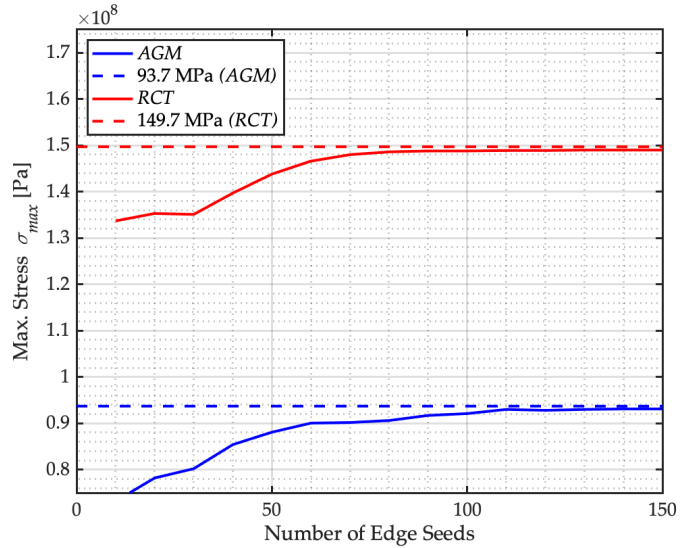


**Figure 3.7:** Convergence of the maximum stress predictions by the FE model for both *AGMs* and *RCTs*.

The FE model predicts only slightly higher stresses than the analytical results, as shown in Table 3.4. This gives confidence in the FE model. Note that the *AGM* model shows a higher discrepancy. The stress predictions are well below the yield stress of $\sigma_y = 440\,\text{MPa}$.

**Table 3.4:** Maximum compressive stress comparison of analytical (AN) and finite element (FE) models.

| Structure | $\sigma_{maxAN}$ [MPa] | $\sigma_{maxFE}$ [MPa] | Discrepancy |
|---|---|---|---|
| *AGMs* | 81.8 | 93.7 | 14.5 % |
| *RCTs* | 136.5 | 149.7 | 9.7 % |

*Eigenvalue Buckling Prediction*
To find the buckling eigenvalues as shown in Figure 3.8, a negative unit gravity load is applied longitudinally, and a 1/3 gravity load is applied laterally with a linear perturbation buckle step in ABAQUS, representing the $-6\,g$ to $2\,g$ ratio of longitudinal and lateral quasi-static loads.
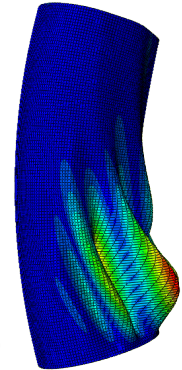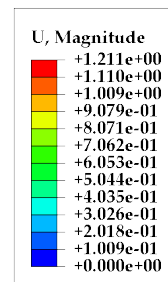


**Figure 3.6:** FE stress distribution prediction on a *RCT* meshed with 100 edge seeds.



**Figure 3.8:** FE first buckling mode eigenvalue prediction on an *AGM* meshed with 150 edge seeds.

This gives an eigenvalue of 244.06 for the first buckling mode of the *AGM* and an eigenvalue of 303.41 for the first buckling mode of the *RCT*. These values are scaled by $6\,g \cdot FS$ to obtain the first mode buckling eigenvalues for the quasi-static load case, as shown in Table 3.5. The eigenvalues are greater than 1, hence the FE models predict no buckling failure for the quasi-static loads.

**Table 3.5:** Buckling eigenvalue analysis results.

| Structure | First Mode Buckling Eigenvalue |
|-----------|--------------------------------|
| *AGMs*    | 1.66                           |
| *RCTs*    | 2.06                           |

The FE models are simplified models of the actual geometry of the structures to allow comparison with the simplified models used for analytical calculations. A more detailed FE model of the actual geometry including end caps is necessary and is discussed in a separate report [4].

## 3.7   Reliability Analysis: Margin of Safety

Having sized the structures based on quasi-static launch loads, objective **(C)** is achieved by analysing the reliability of the structures when subjected to in-orbit loads.

### Margin of Safety
A commonly used measure of the functionality or reliability of a space structure is the margin of safety $MS$ defined by Equation (3.24), where $\sigma_{actual}$ is the stress resulting from a certain load, $\sigma_{allow}$ is the maximum permissible stress before failure and $FS = 2.5$ is the factor of safety. For a given load case, a high value of $MS$ implies high reliability of the structure, whereas $MS < 0$ implies failure [53].

$$MS = \frac{\sigma_{allow}}{FS \cdot \sigma_{actual}} - 1 \qquad (3.24)$$

### Load Case 2: Pressurisation
The stress due to internal pressurisation $p$ of a cylindrical pressure vessel in hoop direction is given by Equation

(3.25) and in longitudinal direction by Equation (3.26). All other symbols have their usual meaning.

$$\sigma_{hoop} = \frac{pr}{t} \quad (3.25) \qquad \sigma_{long} = \frac{pr}{2t} = \frac{\sigma_{hoop}}{2} \qquad (3.26)$$

### Load Case 3: Rotation
When the *AG-Ring* of radius $R$ rotates with an angular velocity $\Omega$, each *AGM* of length $L_{AGM} = 9.8$ m experiences a radially distributed load $f_1$ given by Equation (3.27), where the structural mass $m_s$ and shielding mass $m_{sh}$ are given in Table 3.3 in Section 3.5. The payload mass of one *AGM* is $m_{pay} = 14000$ kg [4].

$$f_1 = \Omega^2 R \frac{\left(m_s + m_{sh} + m_{pay}\right)_{AGM}}{L_{AGM}} \qquad (3.27)$$

$$Y_1 = f_1 \cdot L_{AGM} \qquad (3.28)$$

Assuming that this load is reacted entirely by one *RCT* (or a tether-pair as discussed in Section 4) half-way along $L_{AGM}$, the reaction load $Y_1$ at the *AGM-RCT* interface is given by Equation 3.28. Moreover, the *RCT* experiences a linearly varying distributed load $f_2$ along its length $L_{RCT} = 14$ m given by Equation (3.29), where $y$ is the abscissa starting at the centre of rotation and the structural mass $m_s$ and shielding mass $m_{sh}$ are given in Table 3.3 in Section 3.5. The payload mass of one *RCT* is $m_{pay} = 5000$ kg [4].

$$f_2 = \Omega^2 \frac{\left(m_s + m_{sh} + m_{pay}\right)_{RCT}}{L_{RCT}} y \qquad (3.29)$$

$$Y_2 = \int_{r_b}^{L_{RCT}+r_b} f_2 \, dy + Y_1 \qquad (3.30)$$

Integrating $f_2$ from the radial position of the *RCT* to bearing system interface $r_b = 2.8$ m [52] to the radial position of the *AGM-RCT* interface $L_{RCT} + r_b$ and taking into account $Y1$ gives the reaction force $Y_2$ at the *RCT* to bearing system interface given by Equation (3.30). Performing basic stress analysis, as in Section 3.4, gives the maximum stresses on both structures in Tables 3.6 and 3.7. The same holds for the analysis of *Load Cases 4 and 5*. Having found $\sigma_{actual}$, objective **(C)** is achieved by calculating the $MS$.

**Table 3.6:** Maximum stresses due to on-orbit loads on the *RCTs*.

| Load Case | $\sigma_{actual}$ [MPa] | $\sigma_{allow}$ [MPa] | Failure Mode | $MS$ |
|-----------|------------------------|-----------------------|--------------|------|
| **Load Case 2:** Pressurisation (Hoop) | 26.1 | 440 | Yield | 5.7 |
| **Load Case 2:** Pressurisation (Longitudinal) | 13.1 | 440 | Yield | 12.5 |
| **Load Case 3:** Rotation (Centrifugal Tension) | 5.4 | 440 | Yield | 31.5 |
| **Load Case 4:** Spin-Up (Bending Tension) | 0.0042 | 440 | Yield | 41904 |
| **Load Case 4:** Spin-Up (Bending Compression) | 0.0042 | 136.5 | Buckling | 12999 |
| **Load Case 4:** Spin-Up (Bending Shear) | 0.0002 | 440 | Shear | 740740 |
| **Load Case 5:** Thrust (Bending Tension) | 0.018 | 440 | Yield | 9777 |
| **Load Case 5:** Thrust (Bending Compression) | 0.018 | 136.5 | Buckling | 3033 |
| **Load Case 5:** Thrust (Bending Shear) | 0.0015 | 440 | Shear | 117332 |

**Table 3.7:** Maximum stresses due to on-orbit loads on the *AGMs*.

| Load Case | $\sigma_{actual}$ [MPa] | $\sigma_{allow}$ [MPa] | Failure Mode | $MS$ |
|-----------|------------------------|-----------------------|--------------|------|
| **Load Case 2:** Pressurisation (Hoop) | 37.9 | 440 | Yield | 3.7 |
| **Load Case 2:** Pressurisation (Longitudinal) | 18.9 | 440 | Yield | 8.3 |
| **Load Case 3:** Rotation (Bending Tension) | 4.3 | 440 | Yield | 40 |
| **Load Case 3:** Rotation (Bending Compression) | 4.9 | 81.8 | Buckling | 5.7 |
| **Load Case 3:** Rotation (Bending Shear) | 2.6 | 440 | Shear | 77 |

# 4 Radial Supporting Tethers (RSTs)

## 4.1 Design Loading Conditions

Two *RSTs* run from each *AGM* to the outer edge of the ro-tating bearing system at the Zero Gravity Body at an angle of $\alpha$ = 7.5° out of the rotation plane on each either as shown in Figure 4.1.
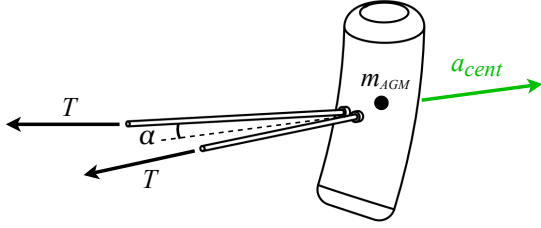


**Figure 4.1:** Tension loads on the *RSTs* due to rotation.

Each tether-pair is sized to withstand centrifugal loads of one *AGM*. Moreover, the tethers of length $L_{RST}$ = 14.25 m are pretensioned with a force of $F_{pre}$ = 1000 N to increase the "breathing mode" resonance frequency from about 2.2 Hz to about 2.8 Hz to avoid oscillations due to live loads on the *AG-Ring* such as astronauts walking within the habi-tat [4]. Other loads due to thrust and spin-up are negligi-ble, especially because a safety factor of $FS$ = 5 is used to size the *RSTs* as recommended by NASA for space tether applications [72]. The tension $T$ in each tether is given by Equation (4.1), where $m_{AGM}$ = 29561 kg is the on-orbit mass of one *AGM* including structural, shielding and payload mass and $a_{cent}$ = $\Omega^2 R$ is the design acceleration. The re-quired cross-section diameter $d$ for a single-line tether with tensile strength $\sigma_y$ is given by Equation (4.2).

$$T = \frac{m_{AGM} a_{cent}}{2\cos\alpha} + F_{pre} = \frac{m_{AGM}\Omega^2 R}{2\cos\alpha} + F_{pre} \qquad (4.1)$$

$$\sigma_y = FS\,\sigma_{applied} = FS\,\frac{4T}{\pi d^2} \implies d = 2\sqrt{\frac{FS \cdot T}{\pi\sigma_y}} \qquad (4.2)$$

## 4.2 Material Selection and Structural Sizing

The mass optimisation is based on choosing a very strong and light material. The material selection is restricted to ultra-high strength plastic fibres commonly suggested for space tether concepts such as the *Space Elevator* [73, 74]. The material index $M_t$ given by Equation (4.3) should be max-imised for tension applications [75].

$$M_t = \frac{\sigma_y}{\rho} \qquad (4.3)$$

**Table 4.1:** Mass comparison of high strength fibres.

| Material | $\sigma_y$ [GPa] | $\rho$ [kg/m$^3$] | $d$ [mm] | $m_{RST}$ [kg] |
|---|---|---|---|---|
| Kevlar | 2.75 | 1440 | 15.5 | 3.86 |
| Zylon | 5.74 | 1550 | 10.7 | 1.99 |
| Spectra | 3.33 | 970 | 14.1 | 2.15 |
| Vectran | 3.15 | 1400 | 14.5 | 3.27 |
| HS Carbon | 4.60 | 1820 | 12.0 | 2.91 |

This is done with the help of an Ashby Chart in Figure 4.2 produced with the CES material selection software [65]. The density $\rho$ and tensile strength $\sigma_y$ of the best perform-ing fibres are listed in Table 4.1 together with the required diameter $d$ and the resulting mass $m_{RST}$ of one *RST*.
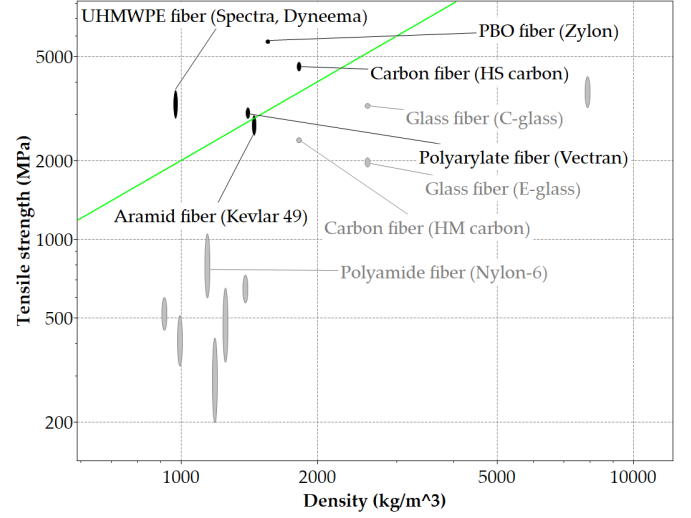


**Figure 4.2:** Ashby chart for $M_t$ with a design guideline of slope 1 (green).

Following objective **(B)**, the final material chosen is Zylon as it gives the lowest mass per tether. Zylon was previously used for the EDL parachute of NASA's Mars Exploration Rover mission.

## 4.3 Reliability Analysis: Survival Probability

Even though *Arceus* will spend most of the mission dura-tion in a low particulate environment, the tethers may be subjected to hypervelocity impacts by micrometeorites and space debris during construction in LEO [76]. Those can cut through tether lines that are significantly larger than the particles. This ratio between particle size $d_{particle}$ and tether diameter $d$ is called lethality coefficient $k_L = \frac{d_{particle}}{d}$. Based on the lower bound from the SEDS-2 experiment [1], this ratio is assumed to be $k_L$ = 0.2. To estimate the lifetime of a single line space tether, the debris and meteoroid parti-cle flux model *ORDEM* [77, 78] is used. For particles larger than a specified diameter $d_{particle}$, this data gives the cumu-lative flux $F(d_{particle})$ as shown by Figure 4.3 on the next page for the construction altitude of 370 km and inclina-tion of 28° as discussed in a seperate report by MTV02 [55]. This gives a flux of $F(d_{particle}) = F(k_L d) = F(2.14\mathrm{e}{-3}\,\mathrm{m}) = 1.918\mathrm{e}{-4}\,\mathrm{m}^{-2}\mathrm{year}^{-1}$ if the standard deviation of the model data $\sigma$ is taken into account, as highlighted in Figure 4.3. The rate of cuts $c$ for the single line tether with diameter $d$ and length $L_{RST}$ is obtained with $c = \pi d L_{RST} F(k_L d)$ [79]. Let $X$ = *Number of cuts on one tether*. The expected number of cuts for a given time $T$ is $N = cT$. Using a Poisson distribu-tion, the probability of $n$ cuts occurring during the time $T$ is given by Equation (4.4).

$$P(X = n) = \frac{(N)^n e^{-N}}{n!} = \frac{(cT)^n e^{-cT}}{n!} \qquad (4.4)$$
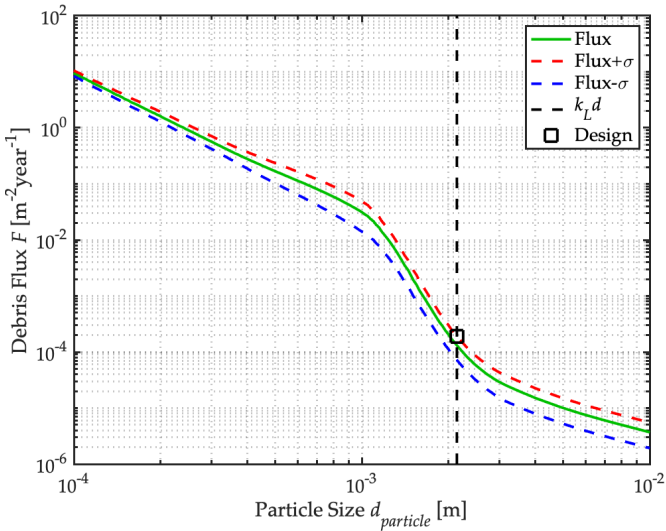
**Figure 4.3:** Cumulative debris flux for particles larger than $d_{particle}$ at an altitude of $370\,km$ and inclination of $28°$ for the year 2040 obtained with *ORDEM*.

The probability of no cuts ($n = 0$), the survival probability, is thus given by Equation (4.5) and is shown in Figure 4.4. Let $Y = $ *Number of cuts on either of the 16 tethers*. The probability of none of the 16 tethers experiencing a cut is given by Equation (4.6) and is shown in Figure 4.4.

$$P(X = 0) = e^{-cT} \quad (4.5) \qquad P(Y = 0) = e^{-16cT} \quad (4.6)$$

For an estimated construction time of $T = 30$ years [42], this gives a survival probability of $P(Y = 0) = 0.957$ which is just above the 95% minimum survival probability requirement according to the NASA Safety Standard [80] for this type of mission. The construction time is an optimistic estimate [42] and could easily go beyond 40 years as explained by MTV02 [42]. The survival probability drops below the limit $P(Y = 0) < 0.95$ after about 35 years.
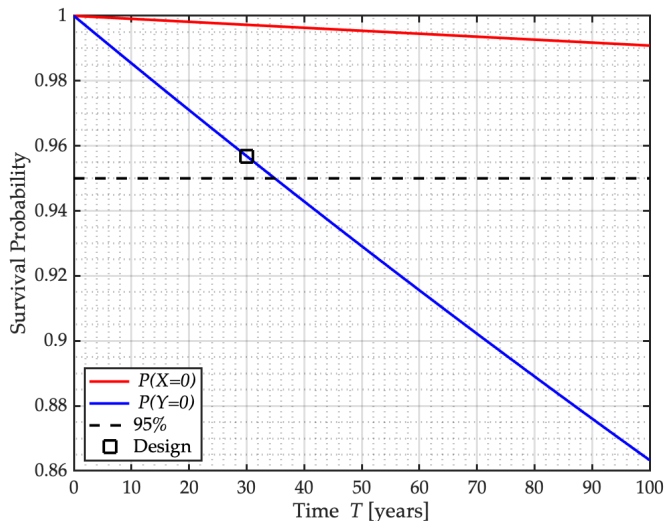


**Figure 4.4:** Survival probabilities of the *RSTs* in LEO.

To improve the survival probability, the tether either needs to have a higher diameter or redundant tension bearing lines distributed over a larger volume [76]. The latter concept is more mass-efficient and thus in line with objective **(B)**, one example being the *Hoytether* [1] shown in Figure

4.5. It consists of $i$ primary and $j$ secondary lines separated into $h$ tether segments. For a tether of length $L$, the length of a primary line is given by $l_i = L/h$. The distance between the primary lines $u$ defines the length of the secondary lines $l_j = 1.005\sqrt{u^2 + l_i}$, where the factor $1.005$ accounts for slack. This multi-line tether structure can suffer many cuts while still providing a continuous tension bearing path without overall tether failure. The effect of these redundancies was verified experimentally by the MAST experiment [81]. Designing Hoytethers for the *AG-Ring* requires an involved design optimisation and further work. However, the increase in mass of a single-line to multi-line tether is estimated as 42 % based on a previous tether design study [82]. This gives a final mass of $m_{RST} = 2.83\,kg$ for one *RST*. Given the tethers' very low mass, the 42 % increase in tether mass is acceptable with regard to objective **(B)**, especially considering the significantly improved reliability.
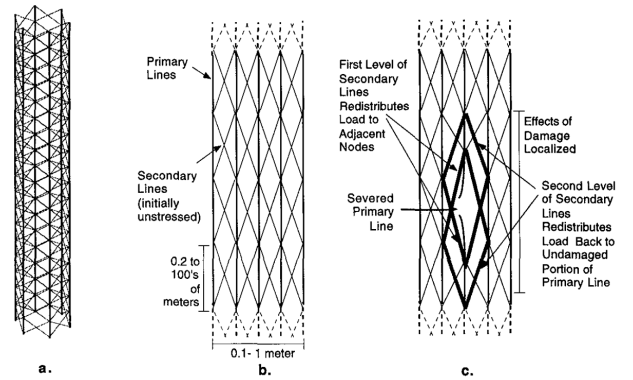


**Figure 4.5:** Hoytether with primary and secondary lines. [1]

# 5  Launch Verification: Vibration Analysis

The primary structures have been sized based on quasi-static loads experienced during launch. However, payloads must also be designed to withstand harmonic, transient and random vibrations as well as thermal, shock, pressure and ground handling loads [83].

*Random Loading and Miles' Equation*
Purely for demonstration purposes, the response due to random vibration on the *AGM* with a lateral frequency of $f_{nY} = 22.3\,Hz$ is analysed. Assume it behaves as a SDOF system and may be characterised by its first mode. It is subjected to a random lateral base acceleration with a power spectral density (PSD) constant for ±1 octave of the natural frequency $f_{nY}$, i.e. in the frequency interval $11.15\,Hz < f < 44.6\,Hz$, with $PSD(f) = 0.06\,g^2/Hz$. In this case, the rms acceleration on the structure $\ddot{x}_{rms}$ is found using the approximation of *Miles's Equation* given by

$$\ddot{x}_{rms} \approx \sqrt{\frac{\pi}{2} Q f_{nY} PSD(f_{nY})} \quad (5.1)$$

where the damping factor is assumed to be $Q = 20$. This yields $\ddot{x}_{rms} \approx 6.5\,g$. A 99 % confidence level is used in practice and gives $\ddot{x}_{99\%} \approx \ddot{x}_{rms} + 3\sigma$, where $\sigma$ is the standard deviation. This can now be used in a quasi-static analysis to find bending moments and stresses on the *AGM* cantilever.

**Table 5.1:** Final mass summary of structural masses $m_s$, shielding masses $m_{sh}$ and payload masses $m_{pay}$ of the *AG-Ring*.

| Structure | $m_s$ [kg] | $m_{sh}$ [kg] [51] | $m_{pay}$ [kg] [4] | $m_s + m_{sh} + m_{pay}$ [kg] | Quantity | Total Overall Mass [kg] |
|---|---|---|---|---|---|---|
| *AGMs* | 1960 | 13601 | 14000 | 29561 | 12 | 354732 |
| *RCTs* | 1625 | 6896 | 5000 | 13521 | 4 | 54084 |
| *RSTs* | 2.83 | - | - | 2.83 | 16 | 45.2 |
| *AG-Ring* | **30065** | **190796** | **188000** | **408861** | **1** | **408861** |

## 6  Discussion

The *AG Design Point* of $R = 19\,\text{m}$ and $\Omega = 5.7\,\text{rpm}$ satisfies both objectives **(A)** and **(B)**. The rotation speed of $\Omega = 5.7\,\text{rpm}$ only has a margin of 5 % from the motion sickness limit. However, the selected comfort limitations are based on relatively old studies. More recent studies show less conservative limits, which could ease the design zone restrictions to allow further mass optimisation. Depending on further investigations of the functional requirements, the structural layout could be adapted to have less *RCTs* which allow transition between the artificial gravity and zero gravity environments of the spacecraft. The mass savings could be significant considering the very high shielding masses for the primary structures.

The primary structures are sized based on quasi-static launch loads only. However, as demonstrated in Section 5, various other launch loads could become the design driver and thus make the sized structures unreliable. These have to be taken into account in the next design iteration to meet objective **(C)**. The chosen alloy Al-8090 results in a 40 % mass reduction compared to the Ti-6Al-4V alloy, making it an excellent choice with respect to objective **(B)**. Whilst cost optimisation is only listed as a secondary objective, the material indices could be defined with an additional cost parameter $C$. The price of the chosen Aluminium alloy Al-8090 is about six times as high as the one for conventional Aluminium alloys such as Al-2024. If cost optimisation becomes a primary objective, the material choice may have to be reconsidered. The chosen semi-monocoque structures have a high structural efficiency with significant mass savings as compared to monocoque structures, but could be improved by a multivariable optimisation of stringer dimensions, stringer ratios and Farrar efficiencies. The performance of different sandwich constructions should be assessed and compared against the current design philosophy. The calculated lateral and longitudinal natural frequencies satisfy the stiffness requirement at launch. However, the *RCTs* only have a margin of 7.5 % from the minimum lateral frequency requirement. To ensure reliability of the structures, objective **(C)**, the natural frequencies should be compared against results from FE models. The discrepancies between analytical and FE results are likely due to the fact that, the quasi-static loads have been modelled as point loads in the analytical calculations, whereas uniform gravity loads are used in the FE predictions. The analytical analysis assumed straight cylinder shells, whereas the FE analysis accounted for the curvature of the *AGMs* which may explain the higher discrepancy for the *AGMs*. As opposed to the analytical results, the FE model does not account for imperfections, which explains the relatively high buckling mode eigenvalues. Since cylinder shells are extremely sensitive to imperfections, it is very important to account for the effect of imperfection in the next iteration. The smeared stiffener theory only provides a low fidelity model. Discrete stiffeners should be modelled as their individual flexibility have a significant impact on the pre-buckling and buckling response [61]. This would allow a more accurate prediction of local and global buckling interactions. Modelling adjacent structures such as the payload interface is necessary to account for interactions between the structures. The reliability of the structures for different in-orbit load cases and failure modes is quantified with the margin of safety. All margins are well above 0, making the sized structures highly reliable. Combinations of different load cases should be considered in the next iteration to improve on objective **(C)**.

The secondary structures are designed to stiffen the structure and to resist centrifugal loads during rotation. In line with objectives **(B)** and **(C)**, the *RSTs* are sized for minimum mass whilst ensuring a high structural reliability. The high strength fibre Zylon is chosen in the material selection as it results in the lowest mass per tether. The reliability of the tethers is improved by designing them as multi-line tethers, Hoytethers, with multiple redundancies distributed over a large volume. A detailed design of these structures is necessary in the next iteration to quantify the actual positive effect on the reliability of multi-line tethers as opposed to single-line tethers. The tethers may not need as many redundancies if they are constructed towards the end of the construction phase, right before leaving LEO. The mass savings would not be significant as each of the 16 tethers has a mass of only around 3 kg. The out-of plane angle of 7.5° is chosen based on geometric compatibility with the outer dimensions of the rotating bearing system. Increasing this angle and investigating higher pretension values could improve the stiffening effect of the tethers.

## 7  Conclusion

The *Artifical Gravity Ring* of the Mars transit vehicle *Arceus* generates an artificial gravity of 0.7 g to mitigate the adverse effects of weightlessness during the IMPACT mission and to ensure astronaut comfort. The mass of the structure is minimised by choosing an optimum design point within the astronaut comfort design zone; by selecting mass-efficient materials for the given loading conditions; and designing structures with a high structural efficiency such as semi-monocoque modules and high-strength tethers. Their reliability is assessed using the margin of safety and a survival probability analysis. The final mass summary is presented in Table 5.1.

# References

[1] Robert P Hoyt and Robert L Forward. Failsafe multi-strand tether seds technology. 2:1151, 1995.

[2] Gene E Maddux. Stress analysis manual. *Air Force Flight Dynamics Laboratory*, October 1986.

[3] DJ Farrar. The design of compression structures for minimum weight. *The Aeronautical Journal*, 53(467):1041–1052, 1949.

[4] Dominic Lee. Mtv03 - gravity loop design and finite element analysis of the arceus spacecraft. *Department of Aeronautics, Imperial College London*, 2021.

[5] The W Hall. Artificial gravity in theory and practice. *46th International Conference on Environmental Systems*, 2016.

[6] Emily R Morey. Spaceflight and bone turnover: correlation with a new rat model of weightlessness. *Bioscience*, 29(3):168–172, 1979.

[7] Linjie Wang, Zhili Li, Cheng Tan, Shujuan Liu, Jianfeng Zhang, Siyang He, Peng Zou, Weibo Liu, and Yinghui Li. Physiological effects of weightlessness: countermeasure system development for a long-term chinese manned spaceflight. *Frontiers of medicine*, 13(2):202–212, 2019.

[8] Stone Jr and Ralph W. An overview of artificial gravity: Effects on human performance and physiology. *NASA Special Publication*, 1973.

[9] Rudolf Fleischer and Gerhard Trippen. Kayles on the way to the stars. *Springer*, pages 232–245, 2004.

[10] Wernher Von Braun. Crossing the last frontier. *Collier's*, 22:24–31, 1952.

[11] Gerard K O'Neill et al. The high frontier: Human colonies in space. *Morrow*, 1977.

[12] B Kent Joosten. Preliminary assessment of artificial gravity impacts to deep-space vehicle design. Technical report, 2002.

[13] J O'Callaghan. Nautilus x: The multi-purpose nasa spacecraft that could take humans to the moon and beyond. *Space Answers*, 14, 2014.

[14] Timo Frett, Michael Mayrhofer, Johann Schwandtner, Ralf Anken, and Guido Petrat. An innovative short arm centrifuge for future studies on the effects of artificial gravity on the human body. *Microgravity Science and Technology*, 26(4):249–255, 2014.

[15] Thiago Schnaider. Mtv01 - project coordination, systems analysis, and reliability modelling of mars transit vehicle. *Department of Aeronautics, Imperial College London*, 2021.

[16] The W Hall. Inhabiting artificial gravity. *Space Technology Conference and Exposition*, page 4524, 1999.

[17] Theod W Hall. Artificial gravity and the architecture of orbital habitats. *Journal of the British Interplanetary Society*, 52:290–300, 1999.

[18] Theodore W Hall, Barbara Faughnan, and Gregg Maryniak. The architecture of artificial gravity: Mathematical musings on designing for life and motion in a centripetally accelerated environment." space manufacturing 8–energy and materials from space. *Citeseer*, 1991.

[19] The W Hall. Artificial gravity: Why centrifugal force is a bad idea. *ASCEND 2020*, 2020.

[20] The W Hall. Architectural considerations for a minimum mass, minimum energy, artificial gravity environment. Technical report, 2002.

[21] Maxime A Faget and EH Olling. Orbital space stations with artificial gravity. 1968.

[22] Ashton Graybiel. The role of the vestibular organs in space exploration. *National Aeronautics and Space Administration*, 1968.

[23] Satoshi Iwase. Effectiveness of centrifuge-induced artificial gravity with ergometric exercise as a countermeasure during simulated microgravity exposure in humans. *Acta astronautica*, 57(2-8):75–80, 2005.

[24] The W Hall. *The architecture of artificial gravity environments for long-duration space habitation*. PhD thesis, University of Michigan, 1994.

[25] D Bryant Cramer. Physiological considerations of artificial gravity. 1985.

[26] Stone Jr and Ralph W. An overview of artificial gravity. *NASA Special Publication*, 314:23, 1973.

[27] Theodore J Gordon and Robert L Gervais. Critical engineering problems of space stations. *Manned Laboratories in Space*, pages 11–32, 1969.

[28] Robert R Gilruth. Manned space stations-gateway to our future in space. *Springer*, pages 1–10, 1969.

[29] Paul R Hill and Emanuel Schnitzer. Rotating manned space stations. *Astronautics*, 7(9):14–18, 1962.

[30] Carl C Clark and James D Hardy. Gravity problems in manned space stations. *NADC-MA-. United States. Naval Air Development Center, Johnsville, Pa. Aviation Medical Acceleration Laboratory*, pages 1–30, 1961.

[31] The W Hall. Artificial gravity visualization, empathy, and design. page 7321, 2006.

[32] Ashton Graybiel. Some physiological effects of alternation between zero gravity and one gravity. page 2019, 1977.

[33] James R Lackner and Paul DiZio. Adaptation in a rotating artificial gravity environment. *Brain Research Reviews*, 28(1-2):194–202, 1998.

[34] James R Lackner and Paul A DiZio. Adaptation to rotating artificial gravity environments. *Journal of vestibular research*, 13(4-6):321–330, 2003.

[35] E Hoegenauer and K Wagner. Artificial gravity for long duration manned space flight. page 4666, 1994.

[36] Michel Van Pelt. Space tethers and space elevators. *Springer Science & Business Media*, 2009.

[37] Mark Wade. Gemini 11. *Encyclopedia Astronautica*, pages 215–226, 2005.

[38] Gilles Clément and Angeli Bukley. Artificial gravity. *Springer Science & Business Media*, 20, 2007.

[39] Maria Scarpa. Mtv04 - design of an extended kalman filter and a nonlinear attitude controller for arceus mars vehicle. *Department of Aeronautics, Imperial College London*, 2021.

[40] Janna Kapplan. personal correspondance.

[41] Vincenzo Schiavo. Mtv06 - physical and mental challenges of deep space exploration. *Department of Aeronautics, Imperial College London*, 2021.

[42] Haganta Ginting. Mtv02 -logistics of assembly, refuel, and refit of the arceus. *Department of Aeronautics, Imperial College London*, 2021.

[43] Unknown. Ariane 6 user's manual issue 1 revision 0. Technical report, March 2018.

[44] Unknown. Ariane 5 user's manual issue 5 revision 2. Technical report, October 2016.

[45] Unknown. Atlas v launch services user's guide. Technical report, March 2010.

[46] Unknown. Delta iv launch services user's guide. Technical report, June 2013.

[47] Unknown. Falcon user's guide. Technical report, April 2020.

[48] Unknown. Soyuz user's manual issue 2 revision 0. Technical report, March 2012.

[49] Dario Riccobono and Laura Mainini. A feasibility study of an artificial gravity system. *Politecnico di Torino*, 2019.

[50] Maria Abbi. Mtv06 - feasibility of closed ecological systems: Water, food and waste management. *Department of Aeronautics, Imperial College London*, 2021.

[51] Maha Khamlichi. Mtv06 - analysis of the radiation and particulate environments and shielding requirements. *Department of Aeronautics, Imperial College London*, 2021.

[52] George Ge. Mtv03 - structural design for the microgravity environment of the arceus. *Department of Aeronautics, Imperial College London*, 2021.

[53] J Jaap Wijker. Spacecraft structures. *Springer Science & Business Media*, 2008.

[54] Leeran Talker. Mtv04 - attitude determination and control. *Department of Aeronautics, Imperial College London*, 2021.

[55] Ben Rose. Mtv02 - mission analysis of a mars transport vehicle. *Department of Aeronautics, Imperial College London*, 2021.

[56] Lloyd H Donnell. A new theory for the buckling of thin cylinders under axial compression and bending. *Guggenheim Aeronautical Laboratory*, 1934.

[57] SB Batdorf. A simplified method of elastic-stability analysis for thin cylindrical shells. 2-modified equilibrium equation. Technical report, 1947.

[58] Christian Hühne, Raimund Rolfes, Elmar Breitbach, and Jan Teßmer. Robust design of composite cylindrical shells under axial compression—simulation and validation. *Thin-walled structures*, 46(7-9):947–962, 2008.

[59] VI Weingarten, EJ Morgan, and Paul Seide. Elastic stability of thin-walled cylindrical and conical shells under axial compression. *Aiaa Journal*, 3(3):500–505, 1965.

[60] Paul Seide and VICTOR I Weingarten. On the buckling of circular cylindrical shells under pure bending. 1961.

[61] VI Weingarten, P Seide, and JP Peterson. Buckling of thin-walled circular cylinders. nasa sp 8007. *Space Vehicle Design Criteria (Structures)*, 1968.

[62] P Seide, VI Weingarten, and EJ Morgan. The development of design criteria for elastic stability of thin shell structures. Technical report, 1960.

[63] Kian Foh Wilson Wong and Paul Weaver. Prediction of local, global buckling and their interactions on thin circular cylindrical shells. page 1788, 2006.

[64] Michael F Ashby and D Cebon. Materials selection in mechanical design. *MRS Bull*, 30(12):995, 2005.

[65] Mark Frank Ashby. Materials selection software ces edupack. *GRANTA*.

[66] M Holland. Pure bending of beams having initial curvature. *The Aeronautical Journal*, 78(768):570–573, 1974.

[67] Ansel C Ugural and Saul K Fenster. Advanced mechanics of materials and applied elasticity. *Pearson Education*, 2011.

[68] Unknown. Selection of material & structure, lecture notes. *Delft University of Technology, Faculty of Aerospace Engineering*.

[69] Jaap Wijker. *Miles' Equation in Random vibrations: Theory and applications in spacecraft structures design*, volume 248. Springer, 2018.

[70] Gunther Moors, Christos Kassapoglou, Sergio Frascino Müller de Almeida, and Clovis Augusto Eça Ferreira. Weight trades in the design of a composite wing box: effect of various design choices. *CEAS Aeronautical Journal*, 10(2):403–417, 2019.

[71] Lorenzo Iannucci. Preliminary airframe design aerospace structures, chapter 4, airframe design lecture notes. *Department of Aeronautics, Imperial College London*.

[72] Donald D Tomlin, Gwyn C Faile, Kazuo B Hayashida, Cynthia L Frost, Carole Y Wagner, Michael L Mitchell, Jason A Vaughn, and Michael J Galuska. Space tethers: Design criteria. *National Aeronautics and Space Administration, Marshall Space Flight Center*, 1997.

[73] Keith Gittemeier, Clark Hawk, Miria Finckenor, and Ed Watts. Space environmental effects of coated tether materials. page 4433, 2005.

[74] Joseph A Carroll. Tether applications in space transportation. *Acta Astronautica*, 13(4):165–174, 1986.

[75] Michael F Ashby and Di Cebon. Materials selection in mechanical design. *Le Journal de Physique IV*, 3(C7):C7–1, 1993.

[76] Wiley J Larson and James Richard Wertz. Space mission analysis and design. Technical report, 1992.

[77] Jer-Chyi Liou, Mark J Matney, Phillip D Anz-Meador, Donald Kessler, Mark Jansen, and Jeffery R Theall. The new nasa orbital debris engineering model ordem2000. *NASA/TP*, 210780, 2002.

[78] Donald J Kessler. Orbital debris environment for spacecraft in low earth orbit. *Journal of spacecraft and rockets*, 28(3):347–351, 1991.

[79] Robert Forward and Robert Hoyt. Failsafe multiline hoytether lifetimes. page 2890, 1995.

[80] NASA Safety Standard. Guidelines and assessment procedures for limiting orbital debris. *NSS*, 1740:14, 1995.

[81] Robert Hoyt, Tyrel Newton, Ian Barnes, Jack Shepherd, S Scott Frank, Jeff Slostad, Belgacem Jaroux, Robert Twiggs, et al. Early results of the multi-application survivable tether (mast) space tether experiment. 2007.

[82] Joseph A Carroll. Preliminary design of a 1 km/sec tether transport facility. *Final Report on NASA contract NASW-4461*, 78, 1991.

[83] Matthew Santer. Spacecraft structures lecture notes. *Department of Aeronautics, Imperial College London*.

[84] ESA-ESTEC. Ecss-e-st-32-10c rev.2 structural factors of safety for spaceflight hardware. Technical report, 2019.
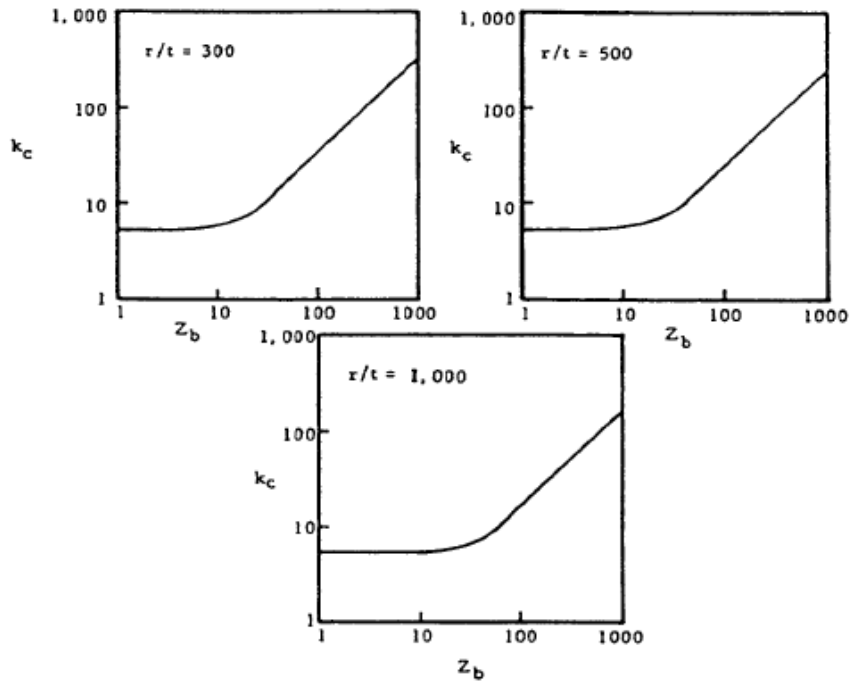
# Appendix A - Design Charts



**Figure 7.1:** Buckling coefficient $k_c$ for curved plates in terms of the length-range parameter $Z_b$. [2]
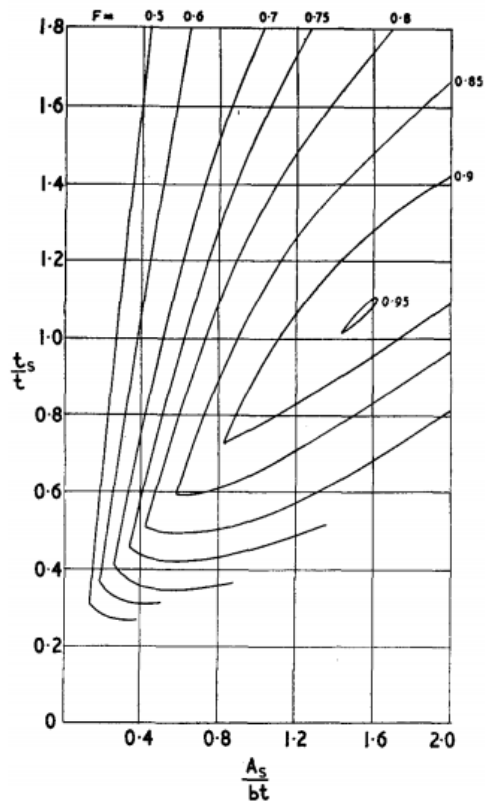


**Figure 7.2:** Farrar efficiency $\mu_F$ contours for Z-stringers with $\frac{c_s}{h_s} = 0.3$. [3]

# Appendix B - Safety Factor Logic

The European Cooperation for Space Standardization (ECSS) [84] defines the safety factors shown in Figure 7.3 and Table 7.1. A project factor of $K_P = 1.5$ set by MTV01 [15], a model factor of $K_M = 1.0$ is chosen from historic data for pressurised systems [84], a local design factor of $K_{LD} = 1.2$ is chosen from historic values for satellites [84]. Since the primary structures are sized for launch, the worst case $FOSU = 1.4$ is chosen as shown in Table 7.1 to give an ultimate design load or safety factor of $DUL = FS = 2.5$.
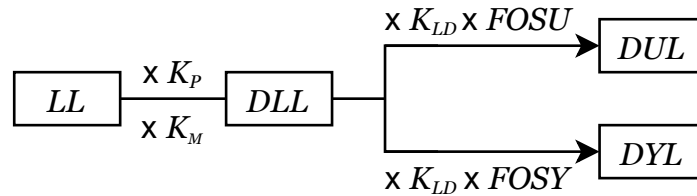


**Figure 7.3:** Safety Factor Logic according to the ECSS "Common Design Logic".

**Table 7.1:** Yield factors of safety $FOSY$ and ultimate factors of safety $FOSU$ for different systems.

| Load Case | $FOSU$ | $FOSY$ |
|---|---|---|
| Metallic parts | Launch 1.4 | Launch 1.25 |
| | Orbit 1.5 | Orbit 1.1 |
| Buckling | 1.4 | na |
| Pressurised Hardware | 1.25 | 1.25 |

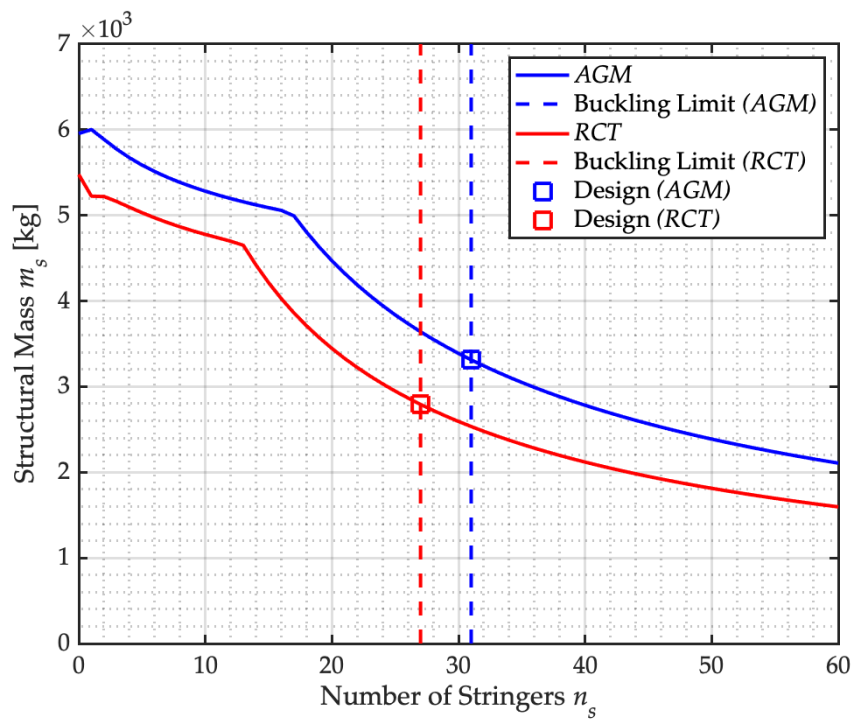## Appendix C - Sizing Results with the Titanium alloy Ti-6Al-4V



**Figure 7.4:** Mass variation with number of stringers for the Titanium alloy Ti-6Al-4V.

# Appendix D - Effect of Tether Pretension on Resonance Frequencies



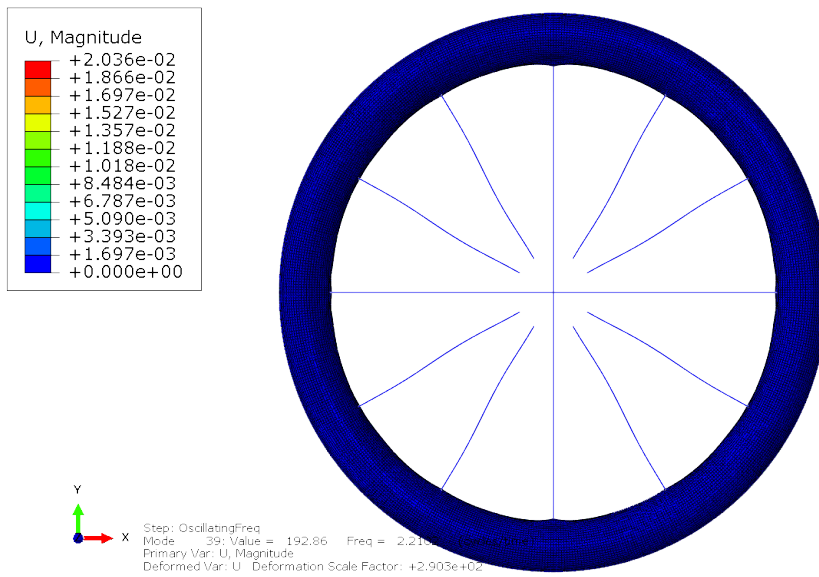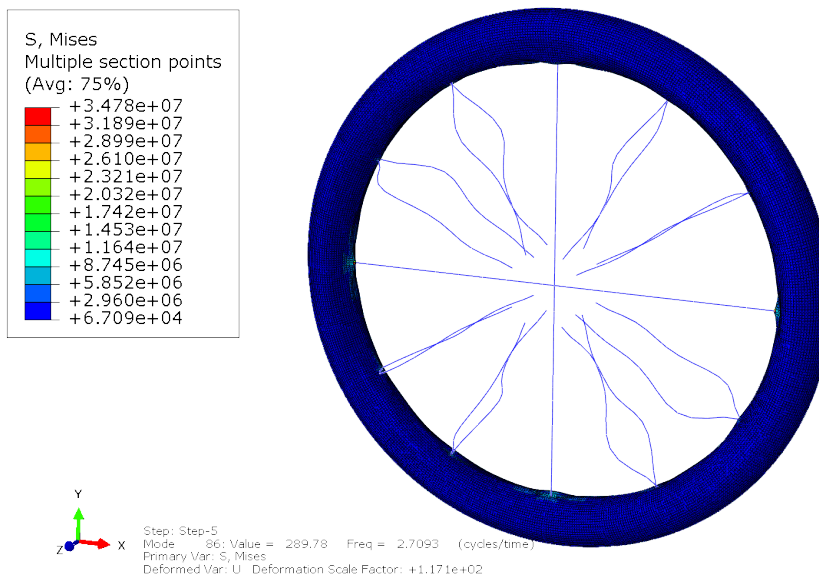**Figure 7.5:** No pretension breathing mode resonant frequencies. [4]



**Figure 7.6:** 1000 N pretension breathing mode resonant frequencies. [4]